

1 **Self-organized canals enable long range directed material transport in bacterial
2 communities**

3

4

5 Ye Li ^{1†}, Shiqi Liu ^{1†}, Yingdan Zhang ², Zi Jing Seng ³, Haoran Xu ¹, Liang Yang ^{2*}, Yilin
6 Wu ^{1*}

7

8

9 ¹ *Department of Physics and Shenzhen Research Institute, The Chinese University of
10 Hong Kong, Shatin, NT, Hong Kong, P.R. China.*

11 ² *School of Medicine, Southern University of Science and Technology, Shenzhen, P.R.
12 China.*

13 ³ *Singapore Center for Environmental Life Science Engineering, Nanyang Technological
14 University, Singapore.*

15

16

17 †These authors contributed equally.

18 *Correspondence: Yilin Wu (ylwu@cuhk.edu.hk) and Liang Yang
19 (yangl@sustech.edu.cn).

20

21

22

23

24

25 **Abstract**

26

27 Long-range material transport is essential to maintain the physiological functions of
28 multicellular organisms such as animals and plants. By contrast, material transport in
29 bacteria is often short-ranged and limited by diffusion. Here we report a unique form of
30 actively regulated long-range directed material transport in structured bacterial
31 communities. Using *Pseudomonas aeruginosa* colonies as a model system, we
32 discover that a large-scale and temporally evolving open channel system spontaneously
33 develops in the colony via shear-induced banding. Fluid flows in the open channels
34 support high-speed (up to 450 $\mu\text{m/s}$) transport of cells and outer membrane vesicles
35 over centimeters, and help to eradicate colonies of a competing species *Staphylococcus*
36 *aureus*. The open channels are reminiscent of human-made canals for cargo transport,
37 and the channel flows are driven by interfacial tension mediated by cell-secreted
38 biosurfactants. The spatial-temporal dynamics of fluid flows in the open channels are
39 qualitatively described by flow profile measurement and mathematical modeling. Our
40 findings demonstrate that mechanochemical coupling between interfacial force and
41 biosurfactant kinetics can coordinate large-scale material transport in primitive life forms,
42 suggesting a new principle to engineer self-organized microbial communities.

43 **Introduction**

44

45 Long-range directed material transport is essential to maintain the physiological
46 functions of multicellular organisms; it helps an organism to transport nutrients,
47 metabolic wastes and signaling molecules, to translocate differentiated sub-populations
48 through the body, and to maintain pH or temperature homeostasis. Long-range directed
49 transport in multicellular organisms is primarily driven by pressure-induced advection
50 and by coordinated cilia beating. For example, hydraulic pressure due to active pumping
51 drives the circulation of body fluid in blood and lymph vessel systems of animals (Scallan,
52 Zawieja, Castorena-Gonzalez, & Davis, 2016); transpiration and capillary pressure
53 passively drive the water transport through vascular tissues of plants (Sack & Holbrook,
54 2006); and cilia beating of epithelial cells drives the cerebrospinal fluid flow in brain
55 ventricles (Faubel, Westendorf, Bodenschatz, & Eichele, 2016) as well as mucus flow in
56 the respiratory tract (Huang & Choma, 2015).

57

58 By contrast, material transport in bacterial world is often short-ranged and limited by
59 diffusion (either passive diffusion due to thermal energy or active diffusion due to self-
60 propulsion of motile cells (X.-L. Wu & Libchaber, 2000)). At the single cell level, diffusion
61 governs nutrient uptake and sets a fundamental limit on the size of bacterial cells (Berg,
62 1993; Nelson, 2003; Schulz & Jorgensen, 2001). In bacterial communities, diffusion has
63 been assumed to dominate material transport (Lavrentovich, Koschwanez, & Nelson,
64 2013; PIRT, 1967; Shao et al., 2017); long-range directed material transport is deemed
65 unusual, despite the notion that bacterial communities resemble multicellular organisms
66 in many aspects such as coordinated metabolism, communication, and division of labor
67 (D. D. Lee, Prindle, Liu, & Suel, 2017; Parsek & Greenberg, 2005; Shapiro, 1998; van
68 Gestel, Vlamakis, & Kolter, 2015). Like in animals and plants, any form of long-range
69 directed material transport would undoubtedly bring profound effect to the development,
70 structure, and stress response of bacterial communities. Intriguingly, a few examples of
71 long-range directed transport in bacterial communities were reported in recent years.
72 Among these examples, it was shown that long-range flows were driven by flagellar
73 motility in sediment biofilms (Fenchel & Glud, 1998; Petroff & Libchaber, 2014) and in
74 bacterial colonies (Y. Wu, Hosu, & Berg, 2011; Xu, Dauparas, Das, Lauga, & Wu, 2019),
75 with a typical flow speed comparable to the swimming speed of individual cells; directed
76 transport can also be driven by passive forces such as osmosis and evaporation-

77 induced pressure gradient (Wilking et al., 2013; Y. Wu & Berg, 2012), with a speed of
78 ~0.1-10 $\mu\text{m/s}$. Nonetheless, these forms of directed material transport all appear to lack
79 autonomous regulation at the community level; the transport is either passive (Wilking et
80 al., 2013; Y. Wu & Berg, 2012) or driven by locally interacting cells (Fenchel & Glud,
81 1998; Petroff & Libchaber, 2014; Y. Wu et al., 2011; Xu et al., 2019). Intra-colony
82 channel structures have been identified in a few bacterial species (Davey, Caiazza, &
83 O'Toole, 2003; Drury, Characklis, & Stewart, 1993; Rooney, Amos, Hoskisson, &
84 McConnell, 2020; Stoodley, DeBeer, & Lewandowski, 1994; Xu et al., 2019); these
85 channel structures have a typical persistence length of a few micron to tens of microns,
86 thus not able to support directed transport beyond millimeter scale.

87
88 Here we report a unique form of actively regulated long-range directed transport in
89 structured bacterial communities. Using *Pseudomonas aeruginosa* colonies as a model
90 system (Ramos, Dietrich, Price-Whelan, & Newman, 2010), we discovered that large-
91 scale, time-evolving open channels spontaneously emerge in the colony; these
92 centimeter-long channels with a free surface are referred to as “bacterial canals”. Fluid
93 flows in the bacterial canals support high-speed (up to 450 $\mu\text{m/s}$) transport of cells and
94 outer membrane vesicles over centimeters and help to eradicate colonies of a competing
95 species *Staphylococcus aureus*. The canals presumably emerge via a complex-fluid
96 phenomenon known as shear-induced banding (Divoux, Fardin, Manneville, & Lerouge,
97 2016; Olmsted, 2008). The typical speed of fluid transport in bacterial canals is one to
98 two orders of magnitude higher than those in previously reported forms of bacterial long-
99 range transport (Fenchel & Glud, 1998; Petroff & Libchaber, 2014; Wilking et al., 2013; Y.
100 Wu et al., 2011; Xu et al., 2019). Gene knock-out and physiological experiments show
101 that canal flows are driven by surface tension gradient mediated by the *P. aeruginosa*-
102 produced biosurfactant rhamnolipids (Lang & Wullbrandt, 1999; Müller et al., 2012).
103 Flow profile measurement and mathematical modeling that involves multiple transport
104 processes and quorum-sensing (QS) regulation (Mukherjee & Bassler, 2019) together
105 reveal the spatial-temporal dynamics of fluid flows in bacterial canals. Overall, our
106 findings demonstrate that mechanochemical coupling between interfacial force and
107 biosurfactant kinetics can coordinate large-scale material transport in primitive life forms,
108 advancing the understanding on multicellular microbial behavior and suggesting a new
109 principle to design macroscopic patterns and functions of synthetic microbial
110 communities (Brenner, You, & Arnold, 2008; Chen, Kim, Hirning, Josić, & Bennett, 2015;

111 Kong, Meldgin, Collins, & Lu, 2018; Luo, Wang, Lu, Ouyang, & You, 2021; Miano, Liao,
112 & Hasty, 2020).

113

114

115 **Results**

116

117 ***P. aeruginosa* colonies establish large-scale open channels supporting directed
118 fluid transport**

119

120 We cultured *P. aeruginosa* PA14 colonies on M9DCAA agar plates (Methods). In the
121 colonies of wildtype and *pilB*-knockout mutant (PA14 $\Delta p i l B$; denoted as nonpiliated
122 mutant), we were intrigued to observe rapid cellular flows streaming through the interior
123 of the colonies, while there was little collective directed motion on both sides of the
124 streams (Movie S1). The streams were tens of microns in width and up to millimeters in
125 length, but their courses were highly unstable presumably due to continuous disruption
126 by cellular motion driven by flagellar motility. On the other hand, for PA14 mutants
127 without flagellar motility, namely PA14 *f lgK*::Tn5 $\Delta p i l A$ (with both flagellar motility and
128 type-IV-pilus mediated motility disabled; denoted by “non-motile *P. aeruginosa*”)
129 (Beaussart et al., 2014) and PA14 *f lgK*::Tn5 (without flagellar motility but with functional
130 type-IV-pilus mediated motility; denoted by “piliated *P. aeruginosa*”)(K. Lee et al., 2011)
131 (Methods), we observed by naked eyes that the colonies of both strains presented many
132 low-cell-density valleys extending from colony center to the edge over centimeters with
133 high directional persistence (Fig. 1A-D). Under the microscope we found that these
134 remarkable, centimeter-long valleys were fluid-filled, free-surface channels (i.e. open
135 channels) ~5-10 μm in height and tens to several hundred μm in width, in which cells
136 carried by the fluid flow streamed rapidly at speeds up to hundreds of $\mu m/s$ in coherent
137 directions (Fig. 1E, Fig. S1A; Movie S2, S3). The fluid flow in channels on average went
138 towards the colony edge and stopped abruptly at the very end (i.e. the tip) of a channel,
139 disappearing into the dense layer of cells near the edge (Fig. S1B; Movie S4). The fluid
140 flow was sensitive to water content in the air environment and it was easily disrupted by
141 decrease of humidity. Cells translocating along the channels eventually settled in near
142 the colony edge and they may contribute to colony expansion; however, channel
143 formation does not necessarily coincide with colony expansion (e.g., see Movie S4).

144 Nearby channels could merge with each other while individual channels could split,
145 resulting in a large-scale channel network across the entire colony (Fig. 1B,D). These
146 large-scale open channels have a free upper surface and therefore, they are distinct
147 from the pipe-like closed channels or conduits previously reported in bacterial colonies
148 (Drury et al., 1993; Rooney et al., 2020; Stoodley et al., 1994; Xu et al., 2019). The
149 open channels we found here are reminiscent of human-made canals for cargo transport,
150 so we refer to these open channels as “bacterial canals”.

151
152 Microscopically, the bacterial canals observed in non-motile (PA14 *flgK*::Tn5 Δ *pilA*) and
153 piliated (PA14 *flgK*::Tn5) *P. aeruginosa* colonies is similar to the unstable streams
154 observed in wildtype *P. aeruginosa* (PA14) and nonpiliated mutant (PA14 Δ *pilB*) colonies,
155 but the former have more stable courses and are thus able to support sustained long-
156 range directed fluid transport. For this reason, and to exclude any potential contribution
157 of flagellar motility to material transport (Y. Wu et al., 2011; Xu et al., 2019), we focused
158 on bacterial canals in this study. When the amount of surface water on agar plates was
159 reduced by extended drying (Methods), the piliated *P. aeruginosa* (PA14 *flgK*::Tn5)
160 colonies displayed a unique branching morphology presumably driven by fingering
161 instability in the presence of surface tension gradient in the colony (Trinschek, John, &
162 Thiele, 2018; Troian, Wu, & Safran, 1989) (Fig. 1F). Interestingly each branch was
163 highly directed and hosted a single canal that ran through the entire branch (Fig. 1F,
164 Movie S5; Fig. S1C, Movie S6). The emergence of canals in such branching colonies
165 occurred robustly at ~8 hr (at 30 °C) or ~15 hr (at room temperature) after inoculation.
166 Since canals in the branching colonies advanced in a predictable manner without
167 merging, hereinafter we systematically characterized canal development and
168 manipulated this process using branching colonies of piliated *P. aeruginosa* (PA14
169 *flgK*::Tn5).

170

171

172 **Canal development requires rhamnolipids and is driven by surface tension
173 gradient**

174

175 *P. aeruginosa* produces the well-characterized biosurfactant (i.e. surface active agents
176 that reduce interfacial energy or surface tension (Chandler, 1987)) rhamnolipids (Lang &
177 Wullbrandt, 1999; Müller et al., 2012). Since canal development does not require cell

178 motility, we hypothesized that surface tension gradient (i.e. Marangoni stress (de
179 Gennes, Brochard-Wyart, & Quere, 2003)) mediated by rhamnolipids provided the
180 driving force for fluid transport in canals; note that the canal flows cannot be driven by
181 osmotic pressure, because osmolarity gradients of cell products (hence the resultant
182 osmotic flows) must be directing towards the colony center. As *in situ* measurement of
183 rhamnolipid concentration or surface tension within colonies and canals is challenging,
184 to examine our hypothesis, we chose to knock out *rhlA* gene (encoding a
185 rhamnosyltransferase essential for the production of rhamnolipids (Ochsner, Fiechter, &
186 Reiser, 1994)) in pilated *P. aeruginosa* (Methods). We found that this rhamnolipid-
187 deficient mutant (PA14 *flgK*::Tn5 $\Delta rhlA$) was unable to develop canals (Fig. 2A); also the
188 colony showed no sign of any mesoscale flows under the microscope. Next, to show
189 that Marangoni stress could drive canal formation, we established artificial surface
190 tension gradient in colonies by injecting an exogenous source of rhamnolipids via a
191 programmable syringe pump (Methods), and it restored canal formation in colonies of
192 the rhamnolipid-deficient mutant (Fig. 2B). We note that the artificial surface tension
193 gradient also promoted colony expansion (Fig. 2B), but again canal formation does not
194 necessarily coincide with colony expansion (see Movie S4 and its legend; also see
195 Discussion). On the other hand, to examine whether canal formation involves agar
196 degradation due to any potential agarase or hydrolase activities, we measured the
197 height profile of the colony and agar with laser scanning confocal microscopy (Methods).
198 We found that while the colony thickness above agar had an abrupt drop near canals,
199 the height of agar under canals and other regions of the colony was uniform and there
200 was no sign of agar degradation (Fig. S2). Taken together, these results show that canal
201 development requires rhamnolipids but not agar degradation, and they provide strong
202 evidence that fluid flows in canals are driven by rhamnolipids-mediated surface tension
203 gradient.

204

205 When we applied a counteracting surface tension gradient directing towards the colony
206 center by placing an agar patch containing surfactant TWEEN 20 (50 mg/mL, surface
207 tension $\sim 4 \times 10^{-2}$ N/m) ~ 1 cm in front of a colony branch, fluid flows in the canal
208 gradually ceased and the canal (but not the colony branch) slowly retracted (Movie S7;
209 Methods), suggesting that the driving force of canal flows is comparable in magnitude to
210 that provided by a surface tension gradient of $\sim 10^3$ mN·m⁻². Moreover, using a
211 previously developed fluorescence reporter $P_{rhlA}\text{-}gfp$ (ASV) for rhamnolipids synthesis

212 (Yang et al., 2009) (GFP-ASV is a short-lived derivative of GFP and its fluorescence
213 intensity reflects the current rate of biosynthesis (Andersen et al., 1998); Methods), we
214 found that the *rhIA* promoter activity was azimuthally symmetric in early-stage colonies
215 and the overall $P_{rhIA}\text{-}gfp(ASV)$ fluorescence increased monotonically until canals
216 emerged (Fig. 2C,D). The result shows that rhamnolipids in the colony center were
217 continuously synthesized, thus generating a radial gradient of surface tension.
218

219 **Flow profiles reveal shear-induced banding and surface tension distribution
220 during canal development**

221
222 The temporal dynamics of fluorescence reporter $P_{rhIA}\text{-}gfp(ASV)$ described in Fig. 2D
223 indicated continuous accumulation of rhamnolipids in the colony center, which would
224 generate a radial surface tension gradient with azimuthal symmetry at the initial stage of
225 canal development. It is then intriguing why rapid flows only emerge in certain regions of
226 the colony (i.e. in canals), even though at the initial stage of canal development every
227 part of the colony at the same distance to the colony center should experience similar
228 Marangoni stress; for instance, canals had already emerged while the colony was still
229 nearly symmetric at T=15 hr in Fig. 2C. Flow speed measurement by particle image
230 velocimetry (PIV) analysis (Methods) in colonies before canals became visible to naked
231 eyes revealed that the flow speed profile in regions with homogeneous cell density
232 distribution displayed flow regimes with distinct shear rates (Fig. 3A,B; Movie S8;
233 Methods). The course of those high-shear-rate domains were initially unstable (Fig. 3C,
234 0-24 min) and similar to the unstable streams observed in wildtype *P. aeruginosa* (PA14)
235 and nonpiliated mutant (PA14 $\Delta pilB$) colonies; as time went by, fluid flows in the high
236 shear domains carried away cells in nearby areas, and the course got widened and
237 gradually became fixed canals (Fig. 3C, 32-56 min; also see Movie S9). The presence
238 of distinct flow regimes under presumably uniform shear stress (Fig. 3A,B) and the
239 instability of flow courses (Fig. 3C) are hallmarks of shear-induced banding, a
240 phenomenon often seen in complex fluids (Divoux et al., 2016; Olmsted, 2008; Ovarlez,
241 Rodts, Chateau, & Coussot, 2009). These results suggest that canals emerge via the
242 onset of shear-induced banding in the colony fluids (see more in Discussion).
243
244 After the onset of canals, due to the coupling of rhamnolipid transport, cellular transport
245 and QS regulation of rhamnolipid synthesis (Lang & Wullbrandt, 1999; Müller et al.,

246 2012), rhamnolipid distribution or surface tension along the canals may vary in space
247 and time, giving rise to a complex and dynamic profile of surface tension gradient that
248 drives fluid flows in canals. To characterize the spatial distribution of surface tension
249 gradient, we sought to measure the flow speed profile in canals because flow speed is
250 linearly proportional to Marangoni stress. PIV analysis as performed in Fig. 3A can only
251 yield the spatially-averaged collective speed, so we switched to local velocity
252 measurement with fluid tracers. In order to avoid perturbing canal flows by introducing
253 external fluid tracers, we took advantage of the fact that some cells being transported
254 along the canals were well isolated from others and these isolated cells could be used
255 as natural fluid tracers. We seeded the colony with a small proportion of GFP(ASV)-
256 expressing cells (PA14 *flgK*::Tn5 *P_{lasB}-gfp*(ASV); Methods), and measured the flow
257 speed in canals by tracking the movement of these fluorescent cells. The speed of cells
258 being transported by canals were too fast to resolve cellular positions in a single image
259 frame, so we computed the time-averaged speed of cells based on the long-exposure-
260 time trajectories of cells in order to reduce the error in speed measurement (Fig. 3D;
261 Methods). The speed of these cells varied significantly along a canal cross-section; it
262 peaked near the canal center and was attenuated near the canal boundaries. We found
263 that the time-averaged peak cell speed near the center of canals was ~200 μm/s (with
264 transient speeds up to 450 μm/s) (Fig. 3D), higher than other reported forms of bacterial
265 long-range directed transport (Fenchel & Glud, 1998; Petroff & Libchaber, 2014; Wilking
266 et al., 2013; Y. Wu et al., 2011; Xu et al., 2019) and most forms of active bacterial
267 motility (Mitchell & Kogure, 2006). Note that the type-IV-pilus mediated motility did not
268 contribute to the movement of these isolated cells being transported in canals, since
269 type-IV-pilus mediated motility requires surface attachment and the resultant speed is
270 only a few μm/s (Talà, Fineberg, Kukura, & Persat, 2019), so the movement of cells
271 indeed followed fluid motion in canals. We further measured the peak flow speed at
272 different locations of canals. As shown by the plateau in Fig. 3E, we found a high-flow-
273 speed region spanning ~20 mm from the canal tip towards the colony center, and the
274 flow speed diminished further towards the colony center. This result reveals the spatial
275 distribution of Marangoni stress and suggests that the surface tension near the colony
276 center has decreased to a steady-state level, presumably due to the saturated
277 concentrations of rhamnolipids there.
278

279 Spatial-temporal dynamics of fluid transport in canals

280

281 Measuring the speed profile as shown in Fig. 3E along a typical ~3-cm long canal is
282 challenging; it requires scanning over at least ~10 locations, with each location taking ~5
283 min and the entire measurement taking >~1 hr (Methods). The trade-off between the
284 large spatial scale of canals (centimeters) and the microscopic nature of speed-profile
285 measurement makes it even more difficult to measure the temporal evolution of canal
286 flows in experiment, so we resorted to mathematical modeling for understanding the
287 spatial-temporal dynamics of canal flows. First of all, we used finite-element simulation
288 of Navier-Stokes equation in a simplified canal geometry (Fig. 4A; Methods) to estimate
289 that the Marangoni stress in canals was on the order of ~1000 mN·m⁻² in order to
290 support a peak flow speed of ~400 μm/s. This magnitude roughly corresponds to the
291 surface tension gradient established between a saturated source of rhamnolipids
292 (surface tension ~30 mN/m; Fig. S3) and a surfactant-free region (surface tension ~70
293 mN/m; Fig. S3) over a distance of ~4 cm, which is consistent with the notion that the
294 colony center has saturated concentrations of rhamnolipids as revealed in Fig. 3E.

295

296 We then built a model to describe the mechanochemical coupling between interfacial
297 force and biosurfactant kinetics, which involve the transport processes of colony
298 constituents (including rhamnolipids, cell mass, QS molecules and nutrients) and QS
299 regulation of rhamnolipid synthesis (Fig. 4B,C; SI Text). Surface tension (γ) is a function
300 of surface density (Γ) of rhamnolipids at the liquid-air interface:

301

$$302 \quad \gamma(\Gamma) = \Pi_{max} \exp(-A\Gamma^2 / \Gamma_c^2) + \gamma_\infty, \quad [1]$$

303

304 where γ_∞ is the surface tension of saturated rhamnolipid solution (at concentration \gg
305 CMC) measured by the pendant drop assay (de Gennes et al., 2003) (Fig. S3), Π_{max} is
306 the difference in surface tension between pure water and the saturated rhamnolipid
307 solution (corresponding to the maximal amount of surface tension decrease due to
308 rhamnolipids), Γ_c is a characteristic surface density of rhamnolipids, and A is a
309 parameter relating bulk rhamnolipid concentration to its steady-state surface density (SI
310 Text). The parameters γ_∞ , Π_{max} in Eq. [1] were obtained by fitting the experimental
311 measurement of the surface tension of rhamnolipid solutions (Fig. S3; SI Text). We
312 introduced dimensionless surface density (Γ_n) and bulk concentration of biosurfactant

313 (c_n) as $\Gamma_n = \Gamma / \Gamma_c$ and $c_n = c / c_s$, which are coupled through the following equations:

314

$$315 \quad \frac{\partial c_n}{\partial t} = \nabla \cdot (D_c \nabla c_n) - (kc_n - kA\Gamma_n^2) + \frac{N}{K_N + N} \alpha_R \rho \frac{B^m}{K_B^m + B^m}, \quad [2]$$

316

$$317 \quad \frac{\partial \Gamma_n}{\partial t} = \nabla \cdot (D_\Gamma \nabla \Gamma_n) - \nabla \cdot [\eta_\Gamma \Gamma_n \nabla \gamma(\Gamma_n)] + (kc_n - kA\Gamma_n^2). \quad [3]$$

318

319 Eq. 2 describes the variation of c_n due to three processes, namely biosurfactant
320 diffusion, biosurfactant exchange between the liquid-air interface and the bulk phase,
321 and biosurfactant production. The biosurfactant exchange between the two phases is a
322 key element in the model (SI Text); it was considered in the analysis of Marangoni flows
323 induced by depositing surfactants into a liquid (Hanyak, Sinz, & Darhuber, 2012; Roché
324 et al., 2014) but rarely in previous studies of the role of surface tension during colony
325 development. The biosurfactant production rate is controlled by nutrient concentration
326 (N), bacterial density (ρ), and QS signal (auto-inducer) concentration (B) (Cao et al.,
327 2016); N , B and ρ follow another set of differential equations (SI Text). Similarly, Eq. 3
328 describes the variation of Γ_n due to biosurfactant diffusion, advective transport of
329 biosurfactant by fluid flows, as well as biosurfactant exchange between the liquid-air
330 interface and the bulk phase; the advective transport term arises because biosurfactant
331 molecules associated with the liquid-air interface are carried along by fluid flows driven
332 by the surface tension gradient $\nabla \gamma$ (de Gennes et al., 2003). In Eq. 2-3, D_Γ , D_c , η_Γ , k ,
333 K_N , α_R , K_B , and m are constant parameters. The details of model equations and
334 parameters are described in SI Text and Table S2.

335

336 As shown by the numerical simulation results based on the model, the distribution of
337 interface-associated surfactant displayed a saturated region near the colony center (Fig.
338 4D) (corresponding to the region with minimal surface tension in Fig. S4A), followed by a
339 biphasic decrease towards the spreading front of the colony (corresponding to the
340 increase of surface tension in Fig. S4A). The resultant surface tension gradient (and
341 therefore flow speed) was nearly zero near the colony center, which agrees with the
342 experimental result (Fig. 3E); further away from the center, it displayed a pronounced
343 plateau (i.e. ranging from the peak to knee of each curve at specific time points,

344 corresponding to the region with rapid canal flows) with modest inclination (Fig. 4E).
345 These results are in qualitative agreement with the measured flow speed profile in
346 canals (Fig. 3E), justifying our model and supporting the notion that canal flows are
347 driven by rhamnolipids-mediated surface tension gradient; note that the modest slope
348 from peak to knee shown in each curve of Fig. 4E was not apparent in Fig. 3E, as it
349 could have been obscured by the large variation of flow speeds measured in
350 experiments or by the low temporal resolution of measurement (scanning over the entire
351 canal takes $>\sim 1$ hr, during which time the true flow speed profile must have shifted and
352 the spatial variation would be smoothed out to certain extent). More importantly, our
353 simulation results were able to reveal that the entire plateau moves away from colony
354 center at a speed of ~ 1 mm/hr, with the width increasing gradually from ~ 20 mm to ~ 30
355 mm in 15 hr while the height decreasing by $\sim 20\%$ (Fig. 4E). Consequently the high-
356 speed directed flows at a specific location in the canal can persist for ~ 20 -30 hr. Taken
357 together, these modeling results provide a qualitative picture how a colony maintains
358 high-speed directed transport along canals for an extended range both in space and
359 time.

360

361 **Directed fluid flows transport outer membrane vesicles and help to eradicate**
362 **competitor colonies**

363

364 Finally we examined whether the canals have other physiological functions besides
365 helping cellular populations to translocate over long distances. *P. aeruginosa* produces
366 outer membrane vesicles (OMVs) to deliver pathogenic factors, antimicrobial
367 compounds, intercellular signals, and public goods that either dissolve poorly or are
368 prone to rapid dilution in the extracellular milieu (Bomberger et al., 2009; Mashburn &
369 Whiteley, 2005; Schwechheimer & Kuehn, 2015). OMVs are slow in diffusion because
370 their sizes are highly heterogeneous ranging from several tens to hundreds of
371 nanometers. To examine whether directed fluid flows in canals can facilitate long-range
372 transport of OMVs produced by *P. aeruginosa*, we isolated OMVs from bacterial culture
373 by centrifugation, labeled them fluorescently, and loaded the OMV dispersion into a
374 canal by microinjection (Methods). We found that these OMVs, having a mean size of
375 ~ 150 nm (Fig. S5), were transported along the canal over centimeter distances (Fig. 5A-
376 C) with a peak speed of >200 μ m/s (Movie S10).

377

378 *P. aeruginosa* is a primary member of poly-species microbial communities found in lung
379 infections of cystic fibrosis (CF) patients, and it may engage in competitive interactions
380 with other species such as *Staphylococcus aureus* (Chew et al., 2018). To examine the
381 potential function of canal flows on interspecies competition, we co-cultured colonies of
382 piliated *P. aeruginosa* (PA14 *flgK*::Tn5) and *S. aureus* on agar plates (Methods). We
383 used *S. aureus* cells harboring a plasmid with constitutive GFP expression (Toledo-
384 Arana et al., 2005), so that the cell mass in *S. aureus* colonies can be quantified by GFP
385 fluorescence during the interaction with *P. aeruginosa* (Methods). We found that *S.*
386 *aureus* colonies irrigated by canal flows were quickly eradicated (Fig. 5D; Movie S11; Fig.
387 S6), with <2% of the initial cell mass remaining after 60 min of contact with canal flows
388 (Fig. 5E, curve labeled as “irrigated”). By contrast, *S. aureus* colonies that were in
389 contact with *P. aeruginosa* colony but did not encounter canal flows retained ~40% of the
390 initial cell mass after 60 min of contact (Fig. 5E, curve labeled as “non-irrigated”). These
391 results demonstrated that fluid flows in canals help to eradicate competing bacterial
392 species. We suggest that canal flows may increase the flux of *P. aeruginosa*-produced
393 antimicrobial substances, such as quinolines encapsulated in OMVs with antibacterial
394 activities against Gram-positive bacteria (Mashburn & Whiteley, 2005) and toxic
395 compounds carried by rhamnolipid micelles (Gdaniec et al., 2022), and therefore
396 enhance the efficiency of inhibiting competing bacterial species. It should be noted that
397 *P. aeruginosa* produces a variety of anti-Staphylococcal compounds such as quinolines,
398 pyocyanin and LasA protease (Hotterbeekx, Kumar-Singh, Goossens, & Malhotra-
399 Kumar, 2017). While hydrophobic substances such as quinolines are poorly diffusible
400 within the colony, those hydrophilic substances dissolvable in water readily diffuse within
401 the agar substrate and their concentration in canals will fade out in a fraction of a
402 second. In both cases, the anti-Staphylococcal substances cannot directly benefit from
403 canal transport, unless they are adsorbed to or encapsulated by larger particles that are
404 slow in diffusion, such as outer membrane vesicles (OMVs) and surfactant micelles
405 ranging from tens to hundreds of nm in size. Therefore the rapid eradication of *S.*
406 *aureus* colonies was most likely due to substances encapsulated in OMVs (Mashburn &
407 Whiteley, 2005) and rhamnolipid micelles (Gdaniec et al., 2022) that were transported by
408 canals.

409

410 **Discussion**

411

412 We have discovered that *P. aeruginosa* colonies develop a large-scale and temporally
413 evolving free-surface open channel system, which supports high-speed (up to 450 $\mu\text{m/s}$)
414 material transport over centimeters. The open channels, or “bacterial canals” are
415 presumably driven by rhamnolipid-mediated surface tension gradient. They
416 spontaneously emerge in the colony following the onset of shear-induced banding of
417 colony fluids. Our findings present a unique form of long-range directed transport in
418 structured bacterial communities.

419

420 Many bacterial species isolated to date synthesize biosurfactants (Ron & Rosenberg,
421 2001). In surface-associated bacterial communities where interfaces are prevalent
422 (O'Toole & Wong, 2016; Persat et al., 2015), the inhomogeneous synthesis of
423 biosurfactants often result in surface tension gradients (Marangoni stress). Marangoni
424 stress was previously suggested to contribute to the expansion of bacterial colonies
425 (Angelini, Roper, Kolter, Weitz, & Brenner, 2009; Du et al., 2012; Fauvart et al., 2012;
426 Rhodeland, Hoeger, & Ursell, 2020; Trinschek et al., 2018). Our findings present a
427 conceptual advance regarding the potential role of biosurfactant-empowered Marangoni
428 stress: It can act as a spatiotemporally regulated driving force for active long-range
429 directed material transport within structured bacterial communities. In this connection,
430 we emphasize the difference between directed material transport within bacterial
431 colonies and colony expansion. Colony expansion normally does not lead to directed
432 transport of materials within the colony. For example, during swarming of wildtype *P.*
433 *aeruginosa* facilitated by Marangoni stress, the colony expansion speed was $\sim 1 \mu\text{m/s}$
434 (Fauvart et al., 2012), which is one order of magnitude slower than individual cells'
435 random motion (tens of $\mu\text{m/s}$) and consequently, a cell or a passive tracer placed in the
436 colony is expected to undergo diffusive motion with a small drift (Zuo & Wu, 2020) rather
437 than directed transport. Moreover, directed material transport within a colony does not
438 necessarily coincide with colony expansion, and the speed of the two processes could
439 differ by orders of magnitude. For example, self-organized motile rings drive directed
440 transport in sessile bacterial colonies that barely expand (Xu et al., 2019)). In our
441 current study, cell mass transported by canals may contribute to colony expansion but
442 this is not always the case (e.g., see Movie S4); more importantly, the speed of directed
443 transport via canals occurring inside the colony is two orders of magnitude greater than

444 that of typical colony expansion (~200 $\mu\text{m}/\text{s}$ versus ~2 mm/hr). Nonetheless, our work
445 provides an new ingredient (i.e., long-range material transport driven by interfacial
446 mechanics) that will complement existing models such as fingering instability (Trinschek
447 et al., 2018) and colony-growth optimization (Luo et al., 2021) to explain and control
448 pattern formation in expanding *P. aeruginosa* colonies.

449

450 Does canal transport play any role during the colonization of *P. aeruginosa* outside the
451 laboratory? To answer this question we need to look back at the behavior of wildtype *P.*
452 *aeruginosa* in our experiments. As noted earlier, wildtype *P. aeruginosa* colonies also
453 displayed rapid streams within the colony but the streams did not turn into stable and
454 persistent canals (Movie S1). The instability was presumably caused by continuous
455 displacement of cells driven by flagellar motility. Flagellar motility weakens cell-cell
456 adhesion and disrupts the course of high-shear flow regimes, thus preventing the high-
457 shear flow regimes from further developing into more stable courses or canals. We
458 suggest that under certain circumstances where *P. aeruginosa* cells tend to
459 downregulate flagellar motility, such as in the airways of patients with cystic fibrosis
460 (Luzar, Thomassen, & Montie, 1985; Mahenthiralingam, Campbell, & Speert, 1994;
461 Wolfgang, Jyot, Goodman, Ramphal, & Lory, 2004), *P. aeruginosa* could develop canals
462 for material transport in clinical or natural environments. Indeed, another flagellated and
463 biosurfactant-producing bacteria *Serratia marcescens* is able to develop canal-like
464 structures during swarming (Fig. S7), but such structures are only found at the center of
465 the colony where most cells appear to be sessile.

466

467 The presence of distinct flow regimes and the instability of flow courses at the early
468 stage of canal development (Fig. 3A,B) suggest that canals emerge via the onset of
469 shear-induced banding in the colony fluids. This notion points to a novel biological
470 function of shear-induced banding that often occurs in complex fluids such as polymer
471 solutions, surfactant micellar solutions and colloidal suspensions (Divoux et al., 2016;
472 Olmsted, 2008; Ovarlez et al., 2009). To further examine the conditions of shear
473 banding in colony fluids, we measured the flow profiles of bacteria-rhamnolipids mixtures
474 resembling the colony constituents in PDMS microfluidic channels subject to uniform
475 shear stress. Under controlled flow conditions in PDMS microfluidic channels, we found
476 that the cross-sectional flow velocity profile of a mixture of dense bacterial suspension
477 ($\sim 1.35 \times 10^{10}$ cells/mL) and concentrated rhamnolipids [at 10 mg/mL, ~100 times critical

478 miceller concentration (CMC) (Zhao, Shi, Ma, Han, & Zhang, 2018)] was highly
479 asymmetric and signaled shear banding (Fig. S8, panel A); whereas the flow velocity
480 profile of pure cell suspension at the same density or of a mixture of rhamnolipids (10
481 mg/mL) and dense 1.1- μ m microsphere suspension ($\sim 1.9 \times 10^{10}$ particles/mL) was closer
482 to the parabolic profile characteristic of Newtonian fluids (Fig. S8, panel B,C). This result
483 suggests that the onset of shear banding in *P. aeruginosa* colonies preceding canal
484 formation requires the interaction between cells and rhamnolipids (most likely in the form
485 of micelles). The detailed biophysical mechanism of this requirement warrants further
486 investigation as a unique rheological behavior of bacterial active matter (Guo, Samanta,
487 Peng, Xu, & Cheng, 2018; Liu, Shankar, Marchetti, & Wu, 2021; Martinez et al., 2020).

488

489 As amphiphilic molecules with surface active properties evolved well before motility
490 mechanisms in the history of life, the mechanism of directed material transport we
491 uncovered here could have long been employed by microbial communities for the
492 transport of cellular mass and cargos in natural environments such as soils and plant
493 leaves. Canal transport helps translocating cellular populations or slowly-diffusing
494 chemical substances over long distances. This form of active material transport could
495 shape the population structure and mediate stress response of bacterial communities,
496 especially in structured environments with heterogeneous population or chemical
497 distribution. On the other hand, with the advance of synthetic biology, mechanochemical
498 coupling between interfacial force and biosurfactant kinetics (including the synthesis,
499 diffusion, and transport) could become a new strategy to design self-organization and
500 sensory functions in synthetic microbial communities (Brenner et al., 2008; Chen et al.,
501 2015; Kong et al., 2018; Miano et al., 2020). For instance, the mechanism could be
502 exploited to transport drugs and chemical effectors loaded in vesicles in order to control
503 the communication and behavior of synthetic bacterial communities.

504 **Methods**

505

506 **Bacterial strains and plasmids**

507

508 **Bacterial strains.** The following strains were used: wildtype *P. aeruginosa* PA14
509 (having both flagellar and type-IV pilus motilities), piliated *P. aeruginosa* (PA14 *flgK*::Tn5;
510 without flagellar motility but retaining type-IV pilus motility), and nonpiliated *P.*
511 *aeruginosa* (PA14 *ΔpilB*; without type-IV pilus motility but retaining flagellar motility), gifts
512 from Roberto Kolter, Harvard University (K. Lee et al., 2011); non-motile *P. aeruginosa*
513 (PA14 *flgK*::Tn5 *ΔpilA*; without either flagellar or type-IV pilus motility) (Beaussart et al.,
514 2014), a gift from George A. O'Toole, Dartmouth College; *P. aeruginosa* deficient in
515 rhamnolipid production (PA14 *flgK*::Tn5 *ΔrhIA*; see details of strain construction below);
516 *Staphylococcus aureus* clinical strain isolate 15981 harboring a plasmid pSB2019-*gfp*
517 that expresses GFP constitutively (Toledo-Arana et al., 2005); *Serratia marcescens*
518 ATCC 274. Single-colony isolates were grown overnight (~ 13-14 hr) in 10 mL culture
519 tubes (unless otherwise stated) with shaking in LB medium (1% Bacto tryptone, 0.5%
520 yeast extract, 0.5% NaCl) at 30 °C to stationary phase. Overnight cultures were used for
521 inoculating colonies on agar plates.

522

523 **Strain construction.** Primers used below are listed in Table S1. To construct the
524 rhamnolipid deficient strain *P. aeruginosa* PA14 *flgK*::Tn5 *ΔrhIA*, upstream of the *rhIA*
525 gene were amplified with 1-*rhIA*_UpF and 2-*rhIA*_UpR primers. Downstream of *rhIA*
526 gene are amplified with 3-*rhIA*_DownF and 4-*rhIA*_DownR primers. The sequences of
527 *rhIA* were obtained from *Pseudomonas* genome database
528 (<http://www.pseudomonas.com/>). The PCR amplification was performed with Q5 High-
529 Fidelity DNA Polymerase (NEB, USA). Using Gibson Assembly Master Mix (NEB, USA),
530 the two purified flanking PCR fragments (Promega, USA) were assembled with BamHI
531 and HindIII-digested PK18 (Gm^r) suicide vector. 10 µL of the assembled products was
532 transformed to *Escherichia coli* DH5a competent cell by heat shock. Transformants
533 were selected on 60 µg/mL Gm-infused LB Lennox agar plates and the insert size was
534 verified by PCR with Pk18-F and Pk18-R primers using Taq Polymerase (Thermo Fisher,
535 USA). A triparental mating was performed with PA14 *flgK*::Tn5 to generate PA14
536 *flgK*::Tn5 *ΔrhIA* gene deletion, through conjugation together with the aid of RK600 helper
537 plasmid strain. ABTC agar containing 10% sucrose was used for SacB-based

538 counterselection. Mutants were confirmed by *rhlA*_F and *rhlA*_R primers with PAO1
539 gDNA as a control. *rhlAGENE*_F and *rhlAGENE*_R primers were used to check for the
540 presence of *rhlA* gene with PAO1 gDNA as a control.

541

542 **Plasmids.** The rhamnolipid synthesis reporter plasmid pMHRA contains an RlhR-
543 regulated P_{rhlA} -*gfp*(ASV) fusion inserted into the vector pMH391 (Yang et al., 2009). *rhlA*
544 encodes a rhamnosyltransferase essential for the production of rhamnolipid under the
545 control of *rhl* QS system (Ochsner et al., 1994), and is thus a good indicator of *rhl* activity
546 (Yang et al., 2009). GFP-ASV is a short-lived derivative of GFP, which degrades with a
547 half-life < 1 h and is rapidly cleared from cells, thus its fluorescence intensity reflects the
548 current rate of biosynthesis (Andersen et al., 1998). For flow speed measurement in
549 canals, the plasmid pMHLB containing a translational fusion of the P_{lasB} -*gfp*(ASV) was
550 used (Hentzer et al., 2002); *lasB* encodes a virulence factor elastase under the control of
551 LasR (Hentzer et al., 2002) and is homogeneously expressed in the colony with
552 sufficiently bright fluorescence suitable for our tracking method. The plasmids were
553 introduced into PA14 *flgK*::Tn5 by electroporation. The transformants were selected on
554 LB 1.5% agar plates supplemented with gentamicin (50 µg/mL). These plasmids have
555 high copy numbers, so we did not need to add any antibiotics into culture environment to
556 prevent plasmid loss.

557

558

559 Preparation of agar plates for colony growth

560

561 *P. aeruginosa* colonies were grown on 0.5% Difco Bacto agar plates infused with
562 M9DCAA medium (Tremblay & Déziel, 2010)[20 mM NH₄Cl, 12 mM Na₂HPO₄, 22 mM
563 KH₂PO₄, 8.6 mM NaCl, 1mM MgSO₄, 1mM CaCl₂, 11 mM dextrose, and 0.5% (wt/vol)
564 casamino acids (BD Bacto, cat. No. 223050)]. We varied the agar concentration and
565 found that canals develop robustly over a relatively wide range of agar concentration
566 between 0.5% and 1.0% wt/vol (Fig. S9). Above 1.0%, canals were not observed
567 presumably because the cells have difficulty to extract sufficient water to maintain an
568 open-surface liquid film on the agar surface, which is the same underlying reason why
569 most bacteria cannot swarm on agar above 1.0% as swarming also requires maintaining
570 open-surface liquid films (Kearns, 2010). As Ca²⁺ cannot coexist stably with many ions,
571 this medium was prepared and stored in two components: (1) 10X nutrient solution

572 without CaCl_2 , sterilized and stored at room temperature; (2) agar infused with CaCl_2 at
573 $1\frac{1}{9}$ times of the desired concentrations, sterilized and stored in 100 mL aliquots. Before
574 use, the component (2) was melted completely in a microwave oven and cooled to
575 $\sim 60^\circ\text{C}$. For each plate, 18 mL molten component (2) was mixed with 2 mL component
576 (1) and the mixture was poured to a polystyrene petri dish (90 mm diameter, 15 mm
577 height). To quantify cell mass in the colony, the membrane dye FM 4-64 (Thermo Fisher
578 Scientific) was added into the agar plates at a final concentration of 1 $\mu\text{g/mL}$. The plate
579 was swirled gently to ensure surface flatness, and then cooled for 10 min without a lid
580 inside a large Plexiglas (PMMA) box, followed by further drying under laminar airflow for
581 5 min or 20 min (to culture branching colonies). 1 μL overnight culture was used to
582 inoculate colonies at the center of each plate, and the plates were incubated at specified
583 temperatures and $>\sim 95\%$ relative humidity; lowering the humidity will lower the
584 probability of canal formation. The colonies expanded at a steady-state speed of ~ 2
585 mm/hr at 30°C . The emergence of canals in branching colonies of pilated *P.*
586 *aeruginosa* (PA14 *flgK*:Tn5) occurred robustly at ~ 8 hr (at 30°C) or ~ 15 hr (at room
587 temperature) after inoculation. In experiments co-culturing *P. aeruginosa* and *S. aureus*,
588 half of casamino acids in the M9DCAA medium described above was replaced by
589 peptone at a final concentration of 0.25% (wt/vol) in order to support growth of *S.*
590 *aureus*; this medium was referred to as M9DCAAP. The M9DCAAP plates were
591 prepared following the same procedures as described above and incubated at 30°C
592 and $>\sim 95\%$ relative humidity.

593

594 **Imaging colonies and canals**

595

596 The macroscale dynamics of *P. aeruginosa* colony or canal development was monitored
597 and measured in a custom-built imaging incubator made of PMMA ($l \times d \times h$, $1 \times 1 \times 1.2$
598 m). The agar plates were sealed with parafilm before incubation in order to maintain
599 saturated humidity. The temperature of the incubator was maintained at 30°C with a
600 heater controlled by feedback circuits. The inner walls of the incubator were covered
601 with black cloth and the plate was illuminated by an LED strip lining at the bottom part of
602 the side walls. The images of colonies or canals were photographed by a digital single-
603 lens reflex camera (DSLR; Canon 700d) every 5 min during incubation (24 mm for whole
604 plate view or 60 mm for zoomed-in view, aperture f/8, exposure time 1/5 s). The time-
605 lapse imaging and LED illumination were triggered by a custom-programmed

606 microcontroller (Arduino). Phase-contrast microscopy imaging of canal development
607 was performed on an inverted microscope (Nikon TI-E) via a 10X dark phase objective
608 (N.A. 0.25) or a 4X dark phase objective (N.A. 0.13). Recordings were made with an
609 sCMOS camera (Andor Zyla 4.2 PLUS USB 3.0; Andor Technology) or the DSLR
610 camera (Canon 700d; triggered by a custom-programmed Arduino microcontroller).

611

612 **Height profile measurement of the colony and agar with laser scanning confocal**
613 **microscopy**

614

615 Molten M9DCAA 0.6% agar was mixed with 0.5 μm -diameter fluorescent microsphere
616 (FluoSpheres carboxylate-modified, ex/em: 580 nm /605 nm; ThermoFisher F8812) at a
617 final microsphere number density of 3.1×10^{11} particles/mL (~1000-fold dilution of the
618 microsphere solution). 20 mL of the agar-microsphere mixture was poured into a 60-mm
619 diameter petri dish. After the agar solidified, the plate was dried under laminar flow
620 without the lid for 30 min. 1 μL overnight culture of *P. aeruginosa* PA14 *flgK::Tn5*
621 harboring the pMHLB plasmid [with $\text{P}_{lasB}\text{-}gfp$ (ASV), as described above] was inoculated
622 into the center of the agar plate. The plate was then sealed by parafilm and incubated in
623 a 30 °C incubator without humidity control for ~24 hr before observation. The 3D
624 structures of the agar and the bacterial colony near canals were imaged with a Leica
625 SP8 laser scanning confocal microscope via a 10X objective (N.A. 0.30). Green
626 fluorescence acquired from cells in the colony (excitation: 476 nm, emission: 480-550
627 nm) and red fluorescence from the microspheres homogeneously dispersed in agar
628 (excitation: 562 nm, emission: 588-658 nm) provided spatial information of the colony
629 and the agar, respectively. The thickness of optical section was set as 12.85 μm . A total
630 of 71 frames at different vertical positions with an interval of 4.28 μm were scanned to
631 acquire the 3D structures. To compute the height profiles of the colony and the agar, we
632 first obtained the 2D cross-sectional fluorescence intensity distributions in both green
633 and red channels by averaging the 3D fluorescence image over the thickness of the
634 optical section. We then binarized the 2D fluorescence intensity distributions in both
635 channels to determine the boundaries of the colony and the agar, thus obtaining the
636 thickness of the colony and the height profile the agar underneath the colony.

637

638 **Establishing exogenous surface tension gradients**

639

640 Rhamnolipid solution (10 mg/mL) was injected into the colony center of the rhamnolipid-
641 deficient mutant *P. aeruginosa* PA14 *flgK::Tn5 ΔrhlA*, in order to create a surface tension
642 gradient pointing radially outwards. To inject exogenous rhamnolipid solutions into the
643 colony, one microliter of PA14 *flgK::Tn5 ΔrhlA* overnight culture was inoculated at the
644 center of an M9DCAA agar plate, and the plate was incubated for 20 hr at room
645 temperature and >~95% relative humidity. Then the lid was replaced by one with a
646 drilled hole, and 10 mg/mL rhamnolipid solution (rhamnolipids 90%, in solid form, AGAE
647 Technologies; dissolved in M9DCAA medium) loaded in a 100 µL glass microsyringe (W-
648 018107, Shanghai Gauge) was pumped into the center of the colony at the rate of 5
649 µL/hr by a syringe pump (Fusion 200, Chemyx) via a PTFE tube (inner diameter 0.3
650 mm) that passed through the hole in the lid. The chosen rhamnolipid concentration [10
651 mg/mL, ~100 times critical micelle concentration (CMC) (Zhao et al., 2018)] was on the
652 order of maximal rhamnolipid concentration that can be produced by *P. aeruginosa*
653 (Soares Dos Santos, Pereira, & Freire, 2016). The end of the PTFE tube barely touched
654 the upper surface of the colony surface. Images of the colony were taken with a DSLR
655 camera (Canon 700d).

656
657 To apply a counteracting surface tension gradient directing towards the colony center,
658 we placed an agar patch containing surfactant TWEEN 20 (50 mg/mL) in front of a
659 colony branch. To prepare the surfactant-infused agar patches, we supplemented the
660 surfactant Tween 20 (Sigma) to molten M9DCAA 3% agar at a final concentration 50
661 mg/mL, poured 10 mL of this agar into 90 mm petri dishes, and cut out 10 mm x 5 mm
662 rectangular patches after the agar solidified. We placed a piece of the surfactant-infused
663 agar patch at ~1 cm in front of a branch of a *P. aeruginosa* PA14 *flgK::Tn5* colony that
664 had grown for 20 hr at 30 °C. Immediately following the placement of the agar patch, the
665 agar plate was transferred to the stage of an inverted microscope (Nikon Ti-E) and the
666 colony branch was observed via a 4X dark phase objective (N.A. 0.13). Image
667 recordings were made with an sCMOS camera (Andor Zyla 4.2 PLUS USB 3.0; Andor
668 Technology). Control experiments followed the same procedures, except that TWEEN
669 20 solution was replaced by M9DCAA medium when preparing the agar patch.

670
671 **Fluorescence imaging of rhamnolipid synthesis reporter and data processing**

672

673 We measured the synthesis level of rhamnolipids during the early stage of canal

674 development using a fluorescence reporter P_{rhlA} -*gfp(ASV)* for the promoter activity of
675 *rhlA* gene as described above. One microliter of the overnight culture of *P. aeruginosa*
676 PA14 *flgK*::Tn5 hosting the plasmid P_{rhlA} -*gfp(ASV)* was inoculated at the center of an
677 M9DCAA agar plate, and the plate was incubated in a sealed glass box with four
678 beakers (each containing 5 mL DI water) at the corners to maintain saturated humidity.
679 The glass box was then transferred to the motorized stage (HLD117, PRIOR Scientific
680 Instruments) on an inverted microscope (Nikon Ti-E) for imaging at room temperature.
681 Multichannel fluorescent images were acquired with a 4X objective (N.A. 0.13) and an
682 FITC/Texas Red dual-band filter set (excitation: 468/34 nm and 553/24 nm, emission:
683 512/23 nm and 630/91 nm, dichroic: 493 to ~530 nm and 574 to ~700 nm; Semrock, cat.
684 No. GFP/DsRed-A-000) with the excitation light provided by a high-power LED light
685 source (X-Cite XLED1, Excelitas Technologies Corp.). For excitation of GFP, BDX LED
686 lamp module (450-495 nm) was turned on and the exposure time was set as 500 ms.
687 For FM 4-64 excitation, GYX module (540-600 nm) was turned on and the exposure time
688 was set as 5 s. The imaging protocol was executed by a custom-programmed
689 microcontroller (Arduino) through the software NIS Element AR (v 4.51, Nikon). Images
690 were recorded with an sCMOS camera (Andor Zyla 4.2 PLUS USB 3.0; Andor
691 Technology).

692

693 The overall fluorescence count of P_{rhlA} -*gfp(ASV)* reporter and FM 4-64 at the colony
694 center was computed by integrating the fluorescence intensity over the entire inoculum
695 region. For each image stack, the image with the lowest overall fluorescence count was
696 chosen as the background and subtracted from the rest of images in the stack. Different
697 colonies may have different lag times due to slight variation of inoculum size across
698 experiments, but their growth dynamics after the lag time is highly conserved.

699

700 **Measurement of shear banding**

701

702 To observe shear banding in colonies, *P. aeruginosa* PA14 *flgK*::Tn5 hosting the plasmid
703 P_{rhlA} -*gfp(ASV)* was inoculated as described above. To observe shear banding in PDMS
704 microfluidic channels, *P. aeruginosa* PA14 *flgK*::Tn5 was grown in 250 mL glass flasks
705 with shaking in LB medium (1% Bacto tryptone, 0.5% yeast extract, 0.5% NaCl) at 30 °C
706 to a cell density ~2.1 X 10⁹ cells/mL, and the culture was concentrated to ~2.1X10¹⁰
707 cells/mL and resuspended in M9DCAA medium before use. PDMS chips with

708 microfluidic channel was fabricated by standard soft lithography technique (Whitesides,
709 Ostuni, Takayama, Jiang, & Ingber, 2001) and sealed to cleaned glass coverslip. The
710 cross-section of microfluidic channels was rectangular, 1.1 mm in width, 200 μm in
711 height, and 4 cm in length. Fluids (~200 μL) were loaded into a glass syringe and
712 pumped into the microfluidic channels by the syringe pump (Chemtex Fusion 200, Two-
713 channel Syringe Pump Model 07200) via a polytetrafluoroethylene (PTFE) tube (inner
714 diameter 0.41 mm, outer diameter 0.92 mm). Before loading the fluids of interest, fresh
715 M9DCAA medium was preloaded into the channel. For experiments with cell-
716 rhamnolipid mixtures, the concentrated bacterial culture (~2.1X10¹⁰ cells/mL
717 resuspended in M9DCAA medium) was mixed with rhamnolipid stock solution (100
718 mg/mL) at 9:1 ratio (final concentration of rhamnolipids: 10 mg/mL, ~100 times CMC;
719 final cell density: ~1.9X10¹⁰ cells/mL) and injected into the microfluidic channel for
720 observation. For experiments with microsphere-rhamnolipid mixtures, microsphere
721 dispersion (Polybead sulfate, 1.1 μm diameter, Polyscience Inc.) was mixed with
722 rhamnolipid (final concentration of rhamnolipids: 10 mg/mL; final number density of
723 microspheres: ~1.9x10¹⁰ particles/mL). The flow rate was maintained constant during
724 observation, ranging from 3 $\mu\text{L}/\text{min}$ to 5 $\mu\text{L}/\text{min}$.

725
726 The observations were performed on an inverted phase-contrast microscope (Nikon TI-
727 E). Shear banding in colonies was observed with a 20X objective (N.A. 0.45, w.d. 8.2–
728 6.9 mm; Nikon, MRH48230) and experiments in PDMS microfluidic channels was
729 imaged with a 10X objective (N. A. 0.25, w.d. 6.2mm; Nikon). Videos were recorded with
730 an sCMOS camera (Andor Zyla 4.2 PLUS USB 3.0; Andor Technology) at 50fps.
731 Velocity field was computed by performing PIV analysis on phase contrast microscopy
732 image sequences using an open-source package MatPIV 1.6.1 written by J. Kristian
733 Sveen (<https://www.mn.uio.no/math/english/people/aca/jks/matpiv/>). For each pair of
734 consecutive images, the interrogation-window size started at 41.6 $\mu\text{m} \times 41.6 \mu\text{m}$ and
735 ended at 10.4 $\mu\text{m} \times 10.4 \mu\text{m}$ after four iterations. The grid size of the resulting velocity
736 field was 5.2 $\mu\text{m} \times 5.2 \mu\text{m}$.

737

738

739 **Measurement of flow speed in canals**

740

741 In order to avoid perturbing canal flows by introducing external fluid tracers, we used
742 fluorescent cells being transported by canal flows as natural fluid tracers. Note that the
743 type-IV-pilus motility did not contribute to the movement of these cells, since type-IV-
744 pilus motility requires surface attachment and the resultant speed is only a few $\mu\text{m/s}$
745 (Talà et al., 2019). The overnight culture of *P. aeruginosa* PA14 *flgK*:Tn5 harboring the
746 pMHLB plasmid [with P_{lasB} -*gfp*(ASV), as described above], whose GFP(ASV) expression
747 was sufficiently bright and uniform along canals for tracking purposes, was mixed with
748 the overnight culture of PA14 *flgK*:Tn5 at a ratio of 1:100. One microliter of this mixture
749 was inoculated at the center of an M9DCAA agar plate, and the plate was incubated for
750 20 hr at 30 °C and >~95% relative humidity. The fluorescent bacteria were imaged on
751 an upright microscope (ECLIPSE Ni-E; Nikon) via a 40X objective (N.A. 0.75) and a
752 FITC filter cube (excitation: 482/35 nm, emission: 536/40 nm, dichroic: 506 nm long pass
753 filter; FITC-3540C-000, Semrock Inc.), with the excitation light provided by a mercury
754 precentered fiber illuminator (Intensilight, Nikon), and recordings were made with an
755 sCMOS camera (Andor Neo 5.5; Andor Technology).

756
757 Due to the ultrahigh speed (up to hundreds $\mu\text{m/s}$) of cells, resolving the position of
758 tracers (cells) frame by frame requires a very short exposure time (<~10 ms) per frame,
759 but such a short exposure time could not yield sufficient photon count to distinguish cells
760 from the background. To overcome this difficulty we recorded cell trajectories during a
761 long exposure time (0.5~5 s) (Fig. 3D), and computed the average speed of cells during
762 the exposure time. This way allowed us to reduce the error in speed measurement due
763 the ultrafast movement of cells. 50 such recordings were made at each position of the
764 canal to yield sufficient number of cell trajectories. All recordings at a specific position
765 were completed within 5 min from placing the agar plate on microscope stage in order to
766 minimize the effect of evaporation. The images were imported into MATLAB (R2014b,
767 The MathWorks; Natick, Massachusetts, United States). For each trajectory, five points
768 (including the two ends) were selected manually using datacursormode function in
769 MATLAB user interface. The selected points were fitted by quadratic spline interpolation
770 (splineinterp function in MATLAB Curve Fitting Toolbox). The length of the fitted curve
771 was taken as the length of the trajectory, and the average speed of the cell was then
772 calculated as the trajectory length divided by the exposure time. In each measurement,
773 the position of field of view relative to the canal tip was determined by moving the
774 motorized stage of the microscope, with an uncertainty of ~1 mm.

775

776 Numerical simulation of flows in a simplified 3D canal geometry

777

778 To estimate the magnitude of surface tension gradient driving flows in canals, we
779 performed a finite-element simulation of Navier-Stokes equation in a simplified 3D canal
780 geometry using the software COMSOL Multiphysics (COMSOL, Stockholm, Sweden).
781 (Fig. 4A). The 3D simulation domain of the modeled canal was a liquid column with a
782 length of 200 μm and a half-ellipse cross-sectional profile (the major and minor axis
783 being 150 μm and 10 μm , respectively). We assumed a free-slip boundary condition at
784 the upper interface of the domain (liquid-air interface) and non-slip boundary condition at
785 the lower boundary (liquid-solid interface). A surface tension gradient was loaded at the
786 liquid-air interface, while the pressure at both ends of the simulation domain was set as
787 zero. The fluid viscosity was set as 0.012 $\text{Pa} \cdot \text{s}$, accordingly to a rheological
788 measurement of *P. aeruginosa* colony extracts (Fauvert et al., 2012). The simulation
789 was performed with a fine finite element mesh. Final results of stationary solution of
790 Navier-Stokes equation in the simulation domain were imported into MATLAB for data
791 processing. The surface and the bulk flow speed profiles were obtained by averaging
792 the flow speed in regions >50 μm away from both ends.

793

794 Isolation, staining, and imaging of outer membrane vesicles (OMVs)

795

796 To examine whether directed fluid flows in canals can facilitate long-range transport of
797 OMVs produced by *P. aeruginosa*, we isolated OMVs from bacterial culture by
798 centrifugation, labeled them fluorescently, and loaded the OMV dispersion into canals by
799 microinjection. We isolated and stained *P. aeruginosa* OMVs using the following
800 procedures. 200 mL of PA14 *flgK*:Tn5 overnight culture grown in M9DCAA medium
801 was centrifuged at 5000 $\times g$ for 5 min in 50 mL centrifuge tubes. The pellet and the
802 supernatant (containing OMVs) were collected and stored separately. The supernatant
803 was forced to pass through a 0.45 μm syringe filter, yielding a raw OMV dispersion with
804 all particulate matter greater than 0.45 μm in size removed. The raw OMV dispersion
805 was further purified and concentrated by centrifugation at 3000 $\times g$ for 5 min in
806 centrifugal devices with a cut-off molecular weight of 100 kDa (Microsep, Pall
807 Corporation), yielding ~500 μL final OMV dispersion in phosphate-buffered saline (PBS;
808 pH=7.0). The obtained OMV dispersion was then transferred to a glass test tube for

809 fluorescent staining with the membrane dye FM 1-43FX (Cat. No. F35355; Thermo
810 Fisher Scientific). 5 µL of FM 1-43FX stock solution (1 mg/mL in DMSO) was added to
811 the test tube and staining was allowed to proceed for 1 hr in a shaker (30 °C and 180
812 rpm). To remove unreacted dyes, the volume of OMV dispersion in test tube was
813 adjusted to 5.5 mL with PBS, and ~1/3 of the stored bacterial pellet was added to the
814 test tube in order to absorb the unreacted dyes; the test tube was replaced in the shaker
815 (30 °C and 180 rpm) and incubated for 5 min, followed by centrifugation at 3000 x g for 5
816 min. The supernatant (containing fluorescently labeled OMVs) was again adjusted to a
817 volume of ~5.5 mL with PBS and the procedures described above were repeated until
818 using up the stored cell pellet. The resulting supernatant was forced to pass through a
819 0.45 µm syringe filter to remove cells, and then was purified and concentrated by
820 centrifugation with the 100 kDa centrifugal devices as described above, yielding ~200 µL
821 fluorescently labeled OMV dispersion in PBS. The size distribution of OMVs isolated
822 this way was characterized by a particle sizer (NanoSight LM10, Malvern Instruments).
823 The OMVs had a size ranging from ~30 nm to ~600 nm, with a mean size of ~150 nm
824 (Fig. S5).

825
826 Microinjection of OMVs into canals was performed using an XYZ micromanipulator (M-
827 562-XYZ, Newport Corporation) and a 100 µL microsyringe with a glass micropipette (20
828 µm in diameter, fabricated by hand-pulling a 0.5 mm glass capillary tube) attached to it.
829 The setup was installed by the side of the stage of an inverted microscope (Nikon Ti-E),
830 where the petri dish was placed. Prior to microinjection, fluorescently labeled OMV
831 dispersion as described above was loaded into the microsyringe, and the lid of the petri
832 dish was removed. Under the microscope via a 4X dark phase objective (N.A. 0.13), the
833 glass micropipette was positioned to be just above the center of a canal at ~15 mm from
834 the canal tip, and approximately 200 nL of OMV dispersion was dispensed to the canal
835 by pushing the microsyringe. Immediately following the microinjection, the lid of petri
836 dished was replaced, and the transport of OMVs in the canal was imaged using a 10X
837 objective (N.A. 0.25) and a TRITC filter set (excitation: 535/50 nm, emission: 610/75 nm,
838 dichroic: 565 nm long pass filter; Semrock) with the excitation light provided by a
839 mercury precentered fiber illuminator (Intensilight, Nikon). Recordings were made with
840 an sCMOS camera (Andor Zyla 4.2) with an exposure time of 0.1 s (for taking real time
841 videos as shown in Movie S10) or 1 s (for acquiring OMV trajectories as shown in Fig.
842 5C). The final distribution of dispensed OMVs along the canal as shown in Fig. 5A,B

843 was imaged via a 4X objective (N.A. 0.13) with an exposure time of 1 s and the images
844 at different locations were stitched by the software NIS Elements AR.

845

846 **Interaction between *S. aureus* and *P. aeruginosa* colonies**

847

848 We used *S. aureus* cells harboring a plasmid with constitutive GFP expression (Toledo-
849 Arana et al., 2005), so that the cell mass in *S. aureus* colonies can be quantified by GFP
850 fluorescence during the interaction with *P. aeruginosa*. Overnight cultures of *S. aureus*
851 and *P. aeruginosa* PA14 were inoculated at different sides of an M9DCAAP agar plate.
852 After incubating at 30 °C for ~20 hr, the *P. aeruginosa* colony branches were
853 approaching *S. aureus* colonies, and then we moved the plate onto the stage of an
854 inverted microscope (Nikon Ti-E) for imaging. Phase contrast images were acquired
855 with a 4X phase contrast objective (N.A. 0.13). Fluorescence images were acquired with
856 a 10X objective (N.A. 0.25) and a FITC filter set (excitation: 482/35 nm, emission: 536/40
857 nm, dichroic: 506 nm long pass filter; Semrock), with the excitation light provided by an
858 LED light source (X-Cite XLED1, Excelitas Technologies Corp.). To compute
859 fluorescence count in the images, the background (acquired at a region with no cells)
860 was first subtracted from the fluorescent images. To correct for the inhomogeneity of
861 excitation illumination, the illumination intensity field was acquired by taking fluorescence
862 images of a ~100 µm thick 0.55% agar pad infused with 10 µg/ml calcein (C0875,
863 Sigma-Aldrich) that was placed on agar surface under the same imaging setup, and then
864 the background-subtracted fluorescence images was divided by the illumination intensity
865 field. The agar pad was made by solidifying molten agar between two cover glasses. *S.*
866 *aureus* colony biomass was measured by the total background-corrected fluorescence
867 count in the area originally occupied by the colony prior to contact with *P. aeruginosa*.

868 **References**

- 869
- 870 Andersen, J. B., Sternberg, C., Poulsen, L. K., Bjørn, S. P., Givskov, M., & Molin, S.
871 (1998). New Unstable Variants of Green Fluorescent Protein for Studies of Transient
872 Gene Expression in Bacteria. *Applied and Environmental Microbiology*, 64(6), 2240-
873 2246. doi: doi:10.1128/AEM.64.6.2240-2246.1998
- 874 Angelini, T. E., Roper, M., Kolter, R., Weitz, D. A., & Brenner, M. P. (2009). *Bacillus*
875 *subtilis* spreads by surfing on waves of surfactant. *Proceedings of the National*
876 *Academy of Sciences*, 106(43), 18109-18113. doi: 10.1073/pnas.0905890106
- 877 Beaussart, A., Baker, A. E., Kuchma, S. L., El-Kirat-Chatel, S., O'Toole, G. A., & Dufrêne,
878 Y. F. (2014). Nanoscale adhesion forces of *Pseudomonas aeruginosa* type IV Pili.
879 *ACS nano*, 8(10), 10723-10733. doi: 10.1021/nn5044383
- 880 Berg, H. C. (1993). *Random Walks in Biology*: Princeton, Princeton, NJ.
- 881 Bomberger, J. M., Maceachran, D. P., Coutermash, B. A., Ye, S., O'Toole, G. A., &
882 Stanton, B. A. (2009). Long-distance delivery of bacterial virulence factors by
883 *Pseudomonas aeruginosa* outer membrane vesicles. *PLoS Pathog*, 5(4), e1000382.
884 doi: 10.1371/journal.ppat.1000382
- 885 Brenner, K., You, L., & Arnold, F. H. (2008). Engineering microbial consortia: a new
886 frontier in synthetic biology. *Trends in Biotechnology*, 26(9), 483-489. doi:
887 <https://doi.org/10.1016/j.tibtech.2008.05.004>
- 888 Cao, Y., Ryser, Marc D., Payne, S., Li, B., Rao, Christopher V., & You, L. (2016).
889 Collective Space-Sensing Coordinates Pattern Scaling in Engineered Bacteria. *Cell*,
890 165(3), 620-630. doi: 10.1016/j.cell.2016.03.006
- 891 Chandler, D. (1987). *Introduction to Modern Statistical Mechanics*: Oxford University
892 Press.
- 893 Chen, Y., Kim, J. K., Hirning, A. J., Josić, K., & Bennett, M. R. (2015). Emergent genetic
894 oscillations in a synthetic microbial consortium. *Science*, 349(6251), 986-989. doi:
895 10.1126/science.aaa3794
- 896 Chew, S. C., Yam, J. K. H., Matysik, A., Seng, Z. J., Klebensberger, J., Givskov, M., . . .
897 Kjelleberg, S. (2018). Matrix Polysaccharides and SiaD Diguanylate Cyclase Alter
898 Community Structure and Competitiveness of *Pseudomonas aeruginosa*
899 during Dual-Species Biofilm Development with *Staphylococcus aureus*.
900 *mBio*, 9(6), e00585-00518. doi: 10.1128/mBio.00585-18
- 901 Davey, M. E., Caiazza, N. C., & O'Toole, G. A. (2003). Rhamnolipid surfactant production

- 902 affects biofilm architecture in *Pseudomonas aeruginosa* PAO1. *J Bacteriol*, 185(3),
903 1027-1036. doi: 10.1128/jb.185.3.1027-1036.2003
- 904 de Gennes, P. G., Brochard-Wyart, F., & Quere, D. (2003). *Capillarity and Wetting
905 Phenomena: Drops, Bubbles, Pearls, Waves*: Springer New York.
- 906 Divoux, T., Fardin, M. A., Manneville, S., & Lerouge, S. (2016). Shear Banding of
907 Complex Fluids. *Annual Review of Fluid Mechanics*, 48(1), 81-103. doi:
908 10.1146/annurev-fluid-122414-034416
- 909 Drury, W. J., Characklis, W. G., & Stewart, P. S. (1993). Interactions of 1 µm latex
910 particles with *Pseudomonas aeruginosa* biofilms. *Water Research*, 27(7), 1119-1126.
- 911 Du, H., Xu, Z., Anyan, M., Kim, O., Leevy, W. M., Shrout, Joshua D., & Alber, M. (2012).
912 High Density Waves of the Bacterium *Pseudomonas aeruginosa* in Propagating
913 Swarms Result in Efficient Colonization of Surfaces. *Biophysical Journal*, 103(3), 601-
914 609. doi: <http://dx.doi.org/10.1016/j.bpj.2012.06.035>
- 915 Faubel, R., Westendorf, C., Bodenschatz, E., & Eichele, G. (2016). Cilia-based flow
916 network in the brain ventricles. *Science*, 353(6295), 176-178. doi:
917 10.1126/science.aae0450
- 918 Fauvert, M., Phillips, P., Bachaspaimayum, D., Verstraeten, N., Fransaer, J., Michiels,
919 J., & Vermant, J. (2012). Surface tension gradient control of bacterial swarming in
920 colonies of *Pseudomonas aeruginosa*. *Soft Matter*, 8(1), 70-76. doi:
921 10.1039/c1sm06002c
- 922 Fenchel, T., & Glud, R. N. (1998). Veil architecture in a sulphide-oxidizing bacterium
923 enhances countercurrent flux. *Nature*, 394(6691), 367-369. doi: 10.1038/28609
- 924 Gdaniec, B. G., Bonini, F., Prodon, F., Braschler, T., Köhler, T., & van Delden, C. (2022).
925 *Pseudomonas aeruginosa* rhamnolipid micelles deliver toxic metabolites and
926 antibiotics into *Staphylococcus aureus*. *iScience*, 25(1), 103669. doi:
927 <https://doi.org/10.1016/j.isci.2021.103669>
- 928 Guo, S., Samanta, D., Peng, Y., Xu, X., & Cheng, X. (2018). Symmetric shear banding
929 and swarming vortices in bacterial superfluids. *Proceedings of the National Academy
930 of Sciences*, 115(28), 7212-7217. doi: 10.1073/pnas.1722505115
- 931 Hanyak, M., Sinz, D. K. N., & Darhuber, A. A. (2012). Soluble surfactant spreading on
932 spatially confined thin liquid films. *Soft Matter*, 8(29), 7660-7671. doi:
933 10.1039/C2SM25484K
- 934 Hentzer, M., Riedel, K., Rasmussen, T. B., Heydorn, A., Andersen, J. B., Parsek, M.
935 R., . . . Givskov, M. (2002). Inhibition of quorum sensing in *Pseudomonas aeruginosa*

- 936 biofilm bacteria by a halogenated furanone compound. *Microbiology (Reading)*,
937 148(Pt 1), 87-102. doi: 10.1099/00221287-148-1-87
- 938 Hotterbeekx, A., Kumar-Singh, S., Goossens, H., & Malhotra-Kumar, S. (2017). In vivo
939 and In vitro Interactions between *Pseudomonas aeruginosa* and *Staphylococcus* spp.
940 *Frontiers in Cellular and Infection Microbiology*, 7(106). doi:
941 10.3389/fcimb.2017.00106
- 942 Huang, B. K., & Choma, M. A. (2015). Microscale imaging of cilia-driven fluid flow.
943 *Cellular and molecular life sciences : CMLS*, 72(6), 1095-1113. doi: 10.1007/s00018-
944 014-1784-z
- 945 Kearns, D. B. (2010). A field guide to bacterial swarming motility. *Nat. Rev. Microbiol.*, 8,
946 634-644.
- 947 Kong, W., Meldgin, D. R., Collins, J. J., & Lu, T. (2018). Designing microbial consortia
948 with defined social interactions. *Nature Chemical Biology*, 14(8), 821-829. doi:
949 10.1038/s41589-018-0091-7
- 950 Lang, S., & Wullbrandt, D. (1999). Rhamnose lipids--biosynthesis, microbial production
951 and application potential. *Appl Microbiol Biotechnol*, 51(1), 22-32. doi:
952 10.1007/s002530051358
- 953 Lavrentovich, M. O., Koschwanez, J. H., & Nelson, D. R. (2013). Nutrient shielding in
954 clusters of cells. *Physical Review E*, 87(6), 062703.
- 955 Lee, D. D., Prindle, A., Liu, J., & Süel, G. M. (2017). SnapShot: Electrochemical
956 Communication in Biofilms. *Cell*, 170(1), 214-214.e211. doi:
957 10.1016/j.cell.2017.06.026
- 958 Lee, K., Hahn, L. D., Yuen, W. W., Vlamakis, H., Kolter, R., & Mooney, D. J. (2011).
959 Metal-Enhanced Fluorescence to Quantify Bacterial Adhesion. *Advanced Materials*,
960 23(12), H101-H104. doi: <https://doi.org/10.1002/adma.201004096>
- 961 Liu, S., Shankar, S., Marchetti, M. C., & Wu, Y. (2021). Viscoelastic control of
962 spatiotemporal order in bacterial active matter. *Nature*, 590(7844), 80-84. doi:
963 10.1038/s41586-020-03168-6
- 964 Luo, N., Wang, S., Lu, J., Ouyang, X., & You, L. (2021). Collective colony growth is
965 optimized by branching pattern formation in *Pseudomonas aeruginosa*. *Molecular*
966 *Systems Biology*, 17(4), e10089. doi: <https://doi.org/10.15252/msb.202010089>
- 967 Luzar, M. A., Thomassen, M. J., & Montie, T. C. (1985). Flagella and motility alterations
968 in *Pseudomonas aeruginosa* strains from patients with cystic fibrosis: relationship to
969 patient clinical condition. *Infect Immun*, 50(2), 577-582. doi: 10.1128/iai.50.2.577-

- 970 582.1985
- 971 Mahenthiralingam, E., Campbell, M. E., & Speert, D. P. (1994). Nonmotility and
972 phagocytic resistance of *Pseudomonas aeruginosa* isolates from chronically
973 colonized patients with cystic fibrosis. *Infect Immun*, 62(2), 596-605. doi:
974 10.1128/iai.62.2.596-605.1994
- 975 Martinez, V. A., Clément, E., Arlt, J., Douarche, C., Dawson, A., Schwarz-Linek, J., . . .
976 Poon, W. C. K. (2020). A combined rheometry and imaging study of viscosity
977 reduction in bacterial suspensions. *Proceedings of the National Academy of Sciences*,
978 117(5), 2326-2331. doi: 10.1073/pnas.1912690117
- 979 Mashburn, L. M., & Whiteley, M. (2005). Membrane vesicles traffic signals and facilitate
980 group activities in a prokaryote. *Nature*, 437, 422-425.
- 981 Miano, A., Liao, M. J., & Hasty, J. (2020). Inducible cell-to-cell signaling for tunable
982 dynamics in microbial communities. *Nature Communications*, 11(1), 1193. doi:
983 10.1038/s41467-020-15056-8
- 984 Mitchell, J. G., & Kogure, K. (2006). Bacterial motility: links to the environment and a
985 driving force for microbial physics. *FEMS Microbiology Ecology*, 55(1), 3-16. doi:
986 10.1111/j.1574-6941.2005.00003.x
- 987 Mukherjee, S., & Bassler, B. L. (2019). Bacterial quorum sensing in complex and
988 dynamically changing environments. *Nature Reviews Microbiology*, 17(6), 371-382.
989 doi: 10.1038/s41579-019-0186-5
- 990 Müller, M. M., Kügler, J. H., Henkel, M., Gerlitzki, M., Hörmann, B., Pöhnlein, M., . . .
991 Hausmann, R. (2012). Rhamnolipids—Next generation surfactants? *Journal of
992 Biotechnology*, 162(4), 366-380. doi: <https://doi.org/10.1016/j.jbiotec.2012.05.022>
- 993 Nelson, P. (2003). *Biological Physics (Updated Edition)*: W. H. Freeman.
- 994 O'Toole, G. A., & Wong, G. C. (2016). Sensational biofilms: surface sensing in bacteria.
995 *Curr Opin Microbiol*, 30, 139-146. doi: 10.1016/j.mib.2016.02.004
- 996 Ochsner, U. A., Fiechter, A., & Reiser, J. (1994). Isolation, characterization, and
997 expression in *Escherichia coli* of the *Pseudomonas aeruginosa* rhlAB genes encoding
998 a rhamnosyltransferase involved in rhamnolipid biosurfactant synthesis. *Journal of
999 Biological Chemistry*, 269(31), 19787-19795.
- 1000 Olmsted, P. D. (2008). Perspectives on shear banding in complex fluids. *Rheologica
1001 Acta*, 47(3), 283-300. doi: 10.1007/s00397-008-0260-9
- 1002 Ovarlez, G., Rodts, S., Chateau, X., & Coussot, P. (2009). Phenomenology and physical
1003 origin of shear localization and shear banding in complex fluids. *Rheologica Acta*,

- 1004 48(8), 831-844. doi: 10.1007/s00397-008-0344-6
- 1005 Parsek, M. R., & Greenberg, E. P. (2005). Sociomicrobiology: the connections between
1006 quorum sensing and biofilms. *Trends Microbiol*, 13(1), 27-33.
- 1007 Payne, S., Li, B., Cao, Y., Schaeffer, D., Ryser, M. D., & You, L. (2013). Temporal control
1008 of self-organized pattern formation without morphogen gradients in bacteria. *Mol Syst
1009 Biol*, 9, 697. doi: 10.1038/msb.2013.55
- 1010 Persat, A., Nadell, C. D., Kim, M. K., Ingremoine, F., Siryaporn, A., Drescher, K., . . .
1011 Stone, H. A. (2015). The mechanical world of bacteria. *Cell*, 161(5), 988-997. doi:
1012 10.1016/j.cell.2015.05.005
- 1013 Petroff, A., & Libchaber, A. (2014). Hydrodynamics and collective behavior of the
1014 tethered bacterium Thiovulum majus. *Proceedings of the National
1015 Academy of Sciences*, 111(5), E537-E545. doi: 10.1073/pnas.1322092111
- 1016 PIRT, S. J. (1967). A Kinetic Study of the Mode of Growth of Surface Colonies of
1017 Bacteria and Fungi. *Microbiology*, 47(2), 181-197. doi: doi:10.1099/00221287-47-2-
1018 181
- 1019 Ramos, I., Dietrich, L. E. P., Price-Whelan, A., & Newman, D. K. (2010). Phenazines
1020 affect biofilm formation by *Pseudomonas aeruginosa* in similar ways at various
1021 scales. *Research in Microbiology*, 161(3), 187-191. doi: 10.1016/j.resmic.2010.01.003
- 1022 Rhodeland, B., Hoeger, K., & Ursell, T. (2020). Bacterial surface motility is modulated by
1023 colony-scale flow and granular jamming. *Journal of The Royal Society Interface*,
1024 17(167), 20200147. doi: doi:10.1098/rsif.2020.0147
- 1025 Roché, M., Li, Z., Griffiths, I. M., Le Roux, S., Cantat, I., Saint-Jalmes, A., & Stone, H. A.
1026 (2014). Marangoni Flow of Soluble Amphiphiles. *Physical Review Letters*, 112(20),
1027 208302. doi: 10.1103/PhysRevLett.112.208302
- 1028 Ron, E. Z., & Rosenberg, E. (2001). Natural roles of biosurfactants. *Environ Microbiol*,
1029 3(4), 229-236.
- 1030 Rooney, L. M., Amos, W. B., Hoskisson, P. A., & McConnell, G. (2020). Intra-colony
1031 channels in *E. coli* function as a nutrient uptake system. *The ISME journal*, 14(10),
1032 2461-2473. doi: 10.1038/s41396-020-0700-9
- 1033 Sack, L., & Holbrook, N. M. (2006). LEAF HYDRAULICS. *Annual Review of Plant
1034 Biology*, 57(1), 361-381. doi: 10.1146/annurev.arplant.56.032604.144141
- 1035 Scallan, J. P., Zawieja, S. D., Castorena-Gonzalez, J. A., & Davis, M. J. (2016).
1036 Lymphatic pumping: mechanics, mechanisms and malfunction. *The Journal of
1037 physiology*, 594(20), 5749-5768. doi: 10.1113/JP272088

- 1038 Schulz, H. N., & Jorgensen, B. B. (2001). Big bacteria. *Annu Rev Microbiol*, 55, 105-137.
1039 doi: 10.1146/annurev.micro.55.1.105
- 1040 Schwechheimer, C., & Kuehn, M. J. (2015). Outer-membrane vesicles from Gram-
1041 negative bacteria: biogenesis and functions. *Nature Reviews Microbiology*, 13(10),
1042 605-619. doi: 10.1038/nrmicro3525
- 1043 Shao, X., Mugler, A., Kim, J., Jeong, H. J., Levin, B. R., & Nemenman, I. (2017). Growth
1044 of bacteria in 3-d colonies. *PLOS Computational Biology*, 13(7), e1005679. doi:
1045 10.1371/journal.pcbi.1005679
- 1046 Shapiro, J. A. (1998). Thinking about bacterial populations as multicellular organisms.
1047 *Annu. Rev. Microbiol.*, 52, 81-104.
- 1048 Soares Dos Santos, A., Pereira, N., Jr., & Freire, D. M. (2016). Strategies for improved
1049 rhamnolipid production by *Pseudomonas aeruginosa* PA1. *PeerJ*, 4, e2078. doi:
1050 10.7717/peerj.2078
- 1051 Stoodley, P., DeBeer, D., & Lewandowski, Z. (1994). Liquid flow in biofilm systems.
1052 *Applied and Environmental Microbiology*, 60(8), 2711-2716.
- 1053 Talà, L., Fineberg, A., Kukura, P., & Persat, A. (2019). *Pseudomonas aeruginosa*
1054 orchestrates twitching motility by sequential control of type IV pili movements. *Nature
1055 Microbiology*, 4(5), 774-780. doi: 10.1038/s41564-019-0378-9
- 1056 Toledo-Arana, A., Merino, N., Vergara-Irigaray, M., Débarbouillé, M., Penadés, J. R., &
1057 Lasa, I. (2005). *Staphylococcus aureus* develops an alternative, ica-independent
1058 biofilm in the absence of the arlRS two-component system. *Journal of Bacteriology*,
1059 187(15), 5318-5329. doi: 10.1128/JB.187.15.5318-5329.2005
- 1060 Tremblay, J., & Déziel, E. (2010). Gene expression in *Pseudomonas aeruginosa*
1061 swarming motility. *BMC Genomics*, 11, 587.
- 1062 Trinschek, S., John, K., & Thiele, U. (2018). Modelling of surfactant-driven front
1063 instabilities in spreading bacterial colonies. *Soft Matter*, 14(22), 4464-4476. doi:
1064 10.1039/C8SM00422F
- 1065 Troian, S. M., Wu, X. L., & Safran, S. A. (1989). Fingering instability in thin wetting films.
1066 *Phys Rev Lett*, 62(13), 1496-1499.
- 1067 van Gestel, J., Vlamakis, H., & Kolter, R. (2015). Division of Labor in Biofilms: the
1068 Ecology of Cell Differentiation. *Microbiol Spectr*, 3(2), Mb-0002-2014. doi:
1069 10.1128/microbiolspec.MB-0002-2014
- 1070 Whitesides, G. M., Ostuni, E., Takayama, S., Jiang, X., & Ingber, D. E. (2001). Soft
1071 lithography in biology and biochemistry. *Annu Rev Biomed Eng*, 3, 335-373.

- 1072 Wilking, J. N., Zaburdaev, V., De Volder, M., Losick, R., Brenner, M. P., & Weitz, D. A.
1073 (2013). Liquid transport facilitated by channels in *Bacillus subtilis* biofilms.
1074 *Proceedings of the National Academy of Sciences*, 110(3), 848-852. doi:
1075 10.1073/pnas.1216376110
- 1076 Wolfgang, M. C., Jyot, J., Goodman, A. L., Ramphal, R., & Lory, S. (2004).
1077 *Pseudomonas aeruginosa* regulates flagellin expression as part of a global response
1078 to airway fluid from cystic fibrosis patients. *Proc Natl Acad Sci U S A*, 101(17), 6664-
1079 6668. doi: 10.1073/pnas.0307553101
- 1080 Wu, X.-L., & Libchaber, A. (2000). Particle diffusion in a quasi-two-dimensional bacterial
1081 bath. *Phys. Rev. Lett.*, 84, 3017-3020.
- 1082 Wu, Y., & Berg, H. C. (2012). Water reservoir maintained by cell growth fuels the
1083 spreading of a bacterial swarm. *Proc Natl Acad Sci U S A*, 109(11), 4128-4133.
- 1084 Wu, Y., Hosu, B. G., & Berg, H. C. (2011). Microbubbles reveal chiral fluid flows in
1085 bacterial swarms. *Proc Natl Acad Sci U S A*, 108(10), 4147-4151.
- 1086 Xu, H., Dauparas, J., Das, D., Lauga, E., & Wu, Y. (2019). Self-organization of swimmers
1087 drives long-range fluid transport in bacterial colonies. *Nature Communications*, 10(1),
1088 1792. doi: 10.1038/s41467-019-09818-2
- 1089 Yang, L., Rybtke, M. T., Jakobsen, T. H., Hentzer, M., Bjarnsholt, T., Givskov, M., &
1090 Tolker-Nielsen, T. (2009). Computer-Aided Identification of Recognized Drugs as
1091 *Pseudomonas aeruginosa* Quorum-Sensing Inhibitors. *Antimicrobial
1092 Agents and Chemotherapy*, 53(6), 2432-2443. doi: 10.1128/aac.01283-08
- 1093 Zhao, F., Shi, R., Ma, F., Han, S., & Zhang, Y. (2018). Oxygen effects on rhamnolipids
1094 production by *Pseudomonas aeruginosa*. *Microbial Cell Factories*, 17(1), 39. doi:
1095 10.1186/s12934-018-0888-9
- 1096 Zuo, W., & Wu, Y. (2020). Dynamic motility selection drives population segregation in a
1097 bacterial swarm. *Proceedings of the National Academy of Sciences*, 117(9), 4693-
1098 4700. doi: 10.1073/pnas.1917789117

1099 **Acknowledgement.** We thank Roberto Kolter (Harvard University) and George A.
1100 O'Toole (Dartmouth College) for providing the bacterial strains; Peter Greenberg
1101 (University of Washington) for helpful comments and for providing bacterial strains; To
1102 Ngai and Hang Jiang (CUHK) for assistance with surface tension measurement;
1103 Shannon Au (CUHK) for help with membrane vesicle isolation; and Bo Zheng and Qi Liu
1104 (CUHK) for help with PDMS microfluidic chip fabrication. We also thank Qihui Hou for
1105 helpful discussion and information on rhamnolipid control of colony patterns. This work
1106 was supported by the National Natural Science Foundation of China (NSFC No.
1107 31971182, to Y.W.), the Research Grants Council of Hong Kong SAR (RGC Ref. No.
1108 14303918, RFS2021-4S04 and CUHK Direct Grants; to Y.W.), Guangdong Natural
1109 Science Foundation for Distinguished Young Scholar (No. 2020B1515020003, to L.Y.),
1110 and Guangdong Basic and Applied Basic Research Foundation (No. 2019A1515110640,
1111 to Y.Z.).

1112

1113

1114 **Author Contributions:** Y.L. designed the study, performed experiments, analyzed and
1115 interpreted the data. S.L. performed experiments, analyzed and interpreted the data.
1116 Y.Z. helped with manuscript preparation. Z.J.S. constructed the *rhlA* mutant. H.X.
1117 performed experiments. L.Y. provided materials and designed the study. Y.W.
1118 conceived and designed the study, analyzed and interpreted the data. L.Y. and Y.W.
1119 supervised the study. Y.W. wrote the paper with input from other authors.

1120

1121

1122 **Competing interests:** The authors declare no competing financial interests.

1123

1124 **Data and materials availability:** All data are available in the main text or the
1125 Supplementary Information.

1126

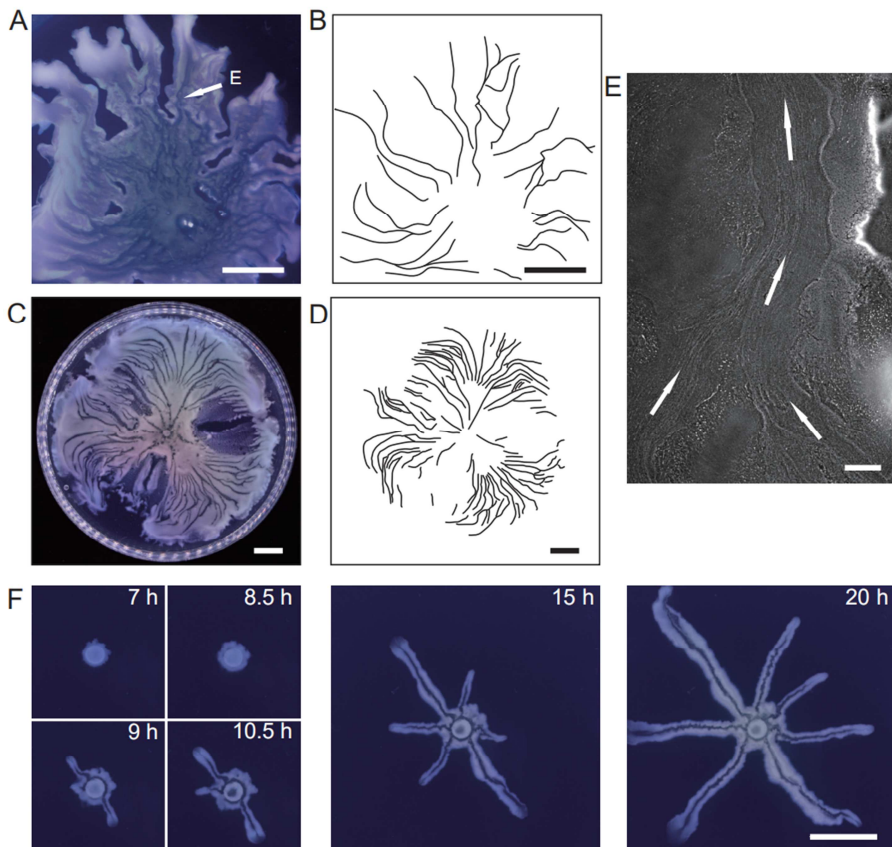
1127

1128 **Figures**

1129

1130 **Figure 1**

1131



1132

1133

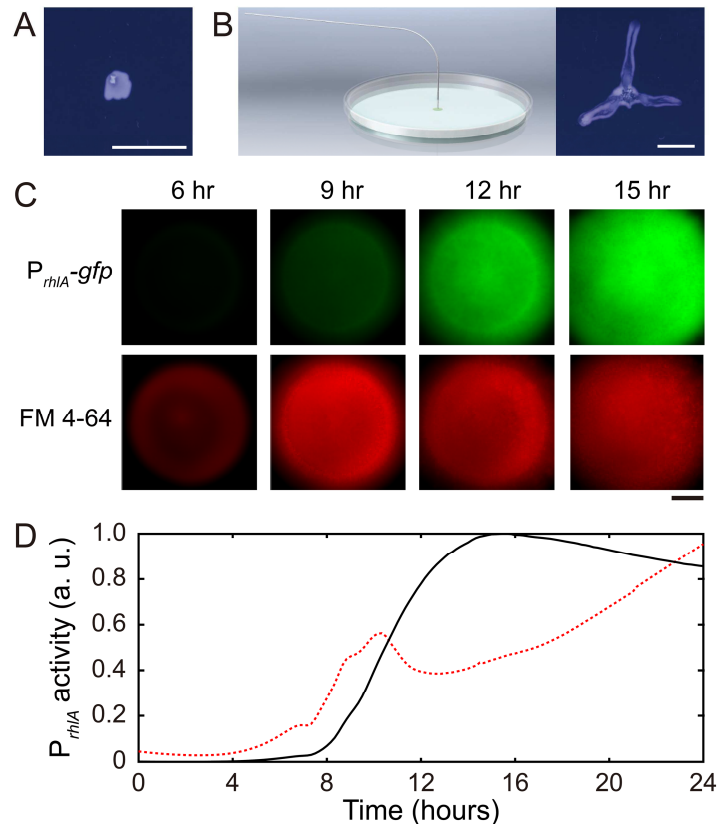
1134 **Fig. 1. Large-scale open channels in non-flagellated *P. aeruginosa* colonies**
1135 **support directed fluid transport.** (A) Colony morphology of non-motile *P. aeruginosa*
1136 (*PA14 flgK::Tn5 ΔpilA*). The arrow indicates the position where the image in panel E
1137 was taken. (B) Sketch of the open channels in panel A for better visualization. (C)
1138 Colony morphology of piliated *P. aeruginosa* (*PA14 flgK::Tn5*). (D) Sketch of the open
1139 channels in panel C for better visualization. Scale bars in A-D, 1 cm. (E) Phase contrast
1140 microscopy image of an open channel with cellular flows in a non-motile *P. aeruginosa*
1141 (*PA14 flgK::Tn5 ΔpilA*) colony, taken at the location indicated by the arrow in panel A.
1142 Arrows indicate flow direction. Scale bar, 100 μ m. Cellular flows in the open channel
1143 are better visualized in Movie S2 because the contrast between the open channel and
1144 other regions is low in still images. (F) Time-lapse image sequence showing the

1145 development of open channels in branching colonies of piliated *P. aeruginosa* (PA14
1146 *flgK::Tn5*). Scale bar, 1 cm. Also see Movie S5.

1147

1148 Figure 2

1149



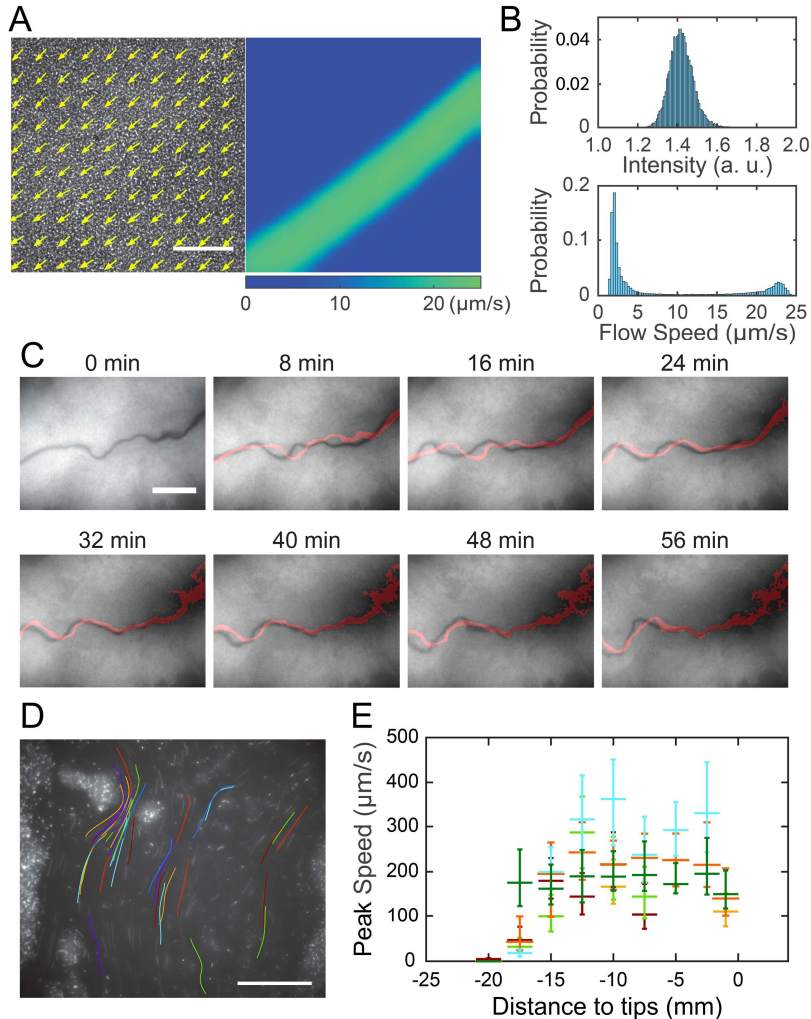
1150

1151 **Fig. 2. Role of rhamnolipids in canal development.** (A) Image of a representative
1152 colony of the rhamnolipid-deficient mutant (PA14 *flgK::Tn5 ΔrhlA*) after 20 hr growth.
1153 The colony failed to develop canals and microscopic flows. (B) Surface tension gradient
1154 established by 1-hr injection of exogenous rhamnolipids at the colony center following
1155 20-hr growth (schematics shown as left panel; Methods) restored the formation of canals
1156 (right panel). Scale bars in A,B, 1 cm. (C) Fluorescence image sequences showing
1157 promoter activity of rhamnolipid synthesis at the early stage of canal development. The
1158 images were taken at the center of representative canal-forming *P. aeruginosa* colonies
1159 (PA14 *flgK::Tn5*) grown at room temperature. The upper row shows GFP(ASV)
1160 fluorescence from the rhamnolipid synthesis reporter $P_{rhlA}-gfp$ (ASV) (Methods), and the
1161 lower row shows red fluorescence of the membrane dye FM 4-64, which serves as a
1162 proxy of cell number in the colony. Scale bar, 1 mm. (D) Temporal dynamics of
1163 rhamnolipid synthesis level measured by the fluorescence of $P_{rhlA}-gfp$ (ASV) reporter
1164 during canal development. Solid and dashed lines represent the overall fluorescence
1165 count of the rhamnolipid synthesis reporter and the FM 4-64 dye, respectively

1166 (Methods). The colony started to expand at $T = \sim 10$ hr, and the expansion caused a
1167 slight drop of overall FM 4-64 fluorescence count during $T = \sim 10\text{-}12$ hr. Three replicate
1168 experiments were performed and they showed the same temporal dynamics.

1169 Figure 3

1170



1171

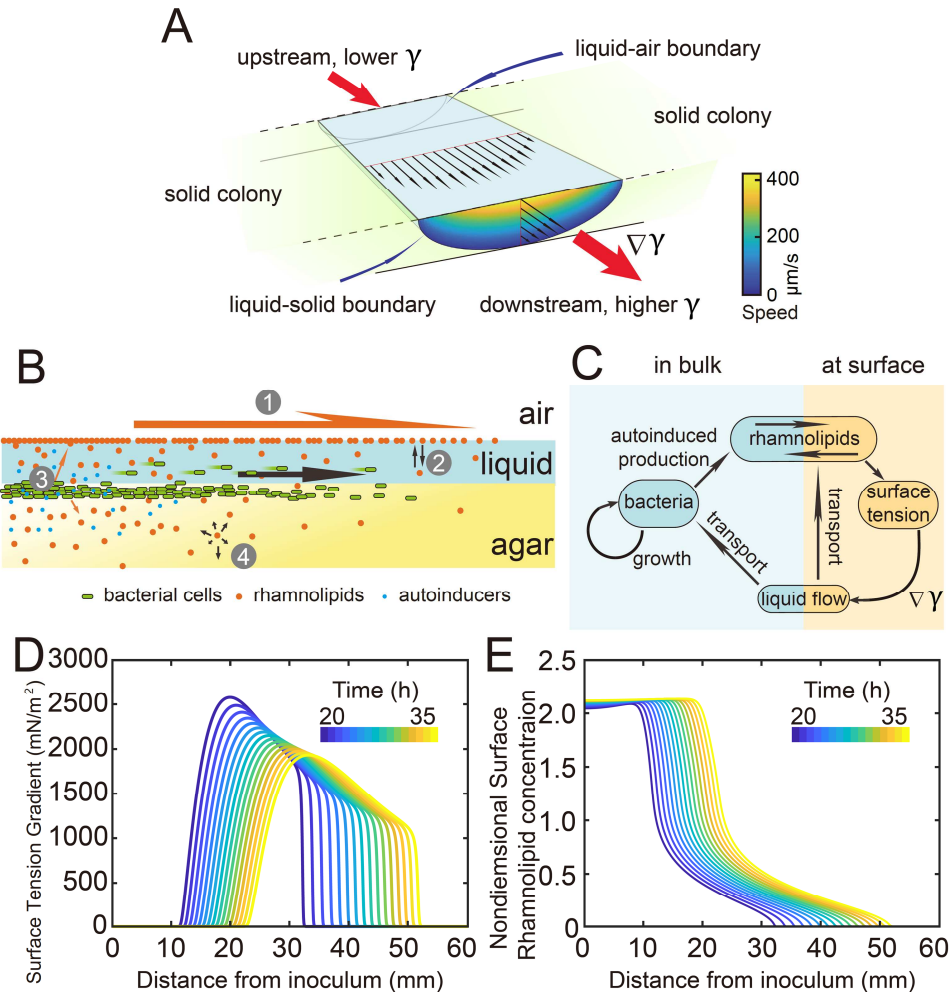
1172

1173 **Fig. 3. Shear-induced banding during canal development and flow speed profile in**
1174 **canals.** (A) Collective velocity field of cells in a region with homogeneous cell density
1175 distribution prior to canal formation. The collective velocity field was measured by
1176 particle image velocimetry (PIV) analysis on phase-contrast image sequence and
1177 averaged over a time window of 4 s (Methods). Arrows in left panel and colormap in
1178 right panel represent collective velocity direction and magnitude, respectively. The
1179 velocity direction field in left panel is superimposed onto the phase-contrast image of this
1180 region. Both panels share the same scale bar (100 μm). Also see Movie S8. (B)
1181 Probability distributions of phase-contrast image intensity (upper panel) and flow speed
1182 (lower panel) associated with panel A. Unimodal distribution of phase-contrast intensity

1183 indicates a homogeneous distribution of cell density. The bimodal distribution of flow
1184 speeds shows the occurrence of a high-speed flow regime. (C) Image sequence
1185 showing the course of a developing canal in a colony. Cells in the colony hosted the
1186 GFP-reporter plasmid expressing $P_{rhlA}\text{-}gfp(ASV)$ and the colony was imaged by
1187 fluorescence microscopy (Methods). The course of the canal (across the center of each
1188 image) had lower cell density due to flushing by rapid flows and thus appeared darker
1189 than other areas. The red trace in each image starting from T= 8 min indicates the
1190 course of the canal in the previous image (8 min earlier). Scale bar, 125 μm . Also see
1191 Movie S9. (D) The fluorescence image of a canal in a *P. aeruginosa* colony seeded with
1192 ~1% GFP-expressing cells. The image was taken at a distance of ~12.5 mm from the tip
1193 of a canal. Colored traces show the trajectories of 38 fluorescent cells being transported
1194 in the canal, which were recorded during 0.5 s exposure time of a single image frame.
1195 Scale bar, 100 μm . Different colors serve to distinguish trajectories of different cells. (E)
1196 Peak flow speed at different locations of canals. The horizontal axis indicates the
1197 distance from the canal tips to the measuring position. Horizontal error bars indicate the
1198 uncertainty of canal position measurement (1 mm). Vertical error bars indicate the full
1199 range of peak speeds measured from >20 cell trajectories. Data from independent
1200 experiments are presented in different colors.

1201 Figure 4

1202



1203

1204

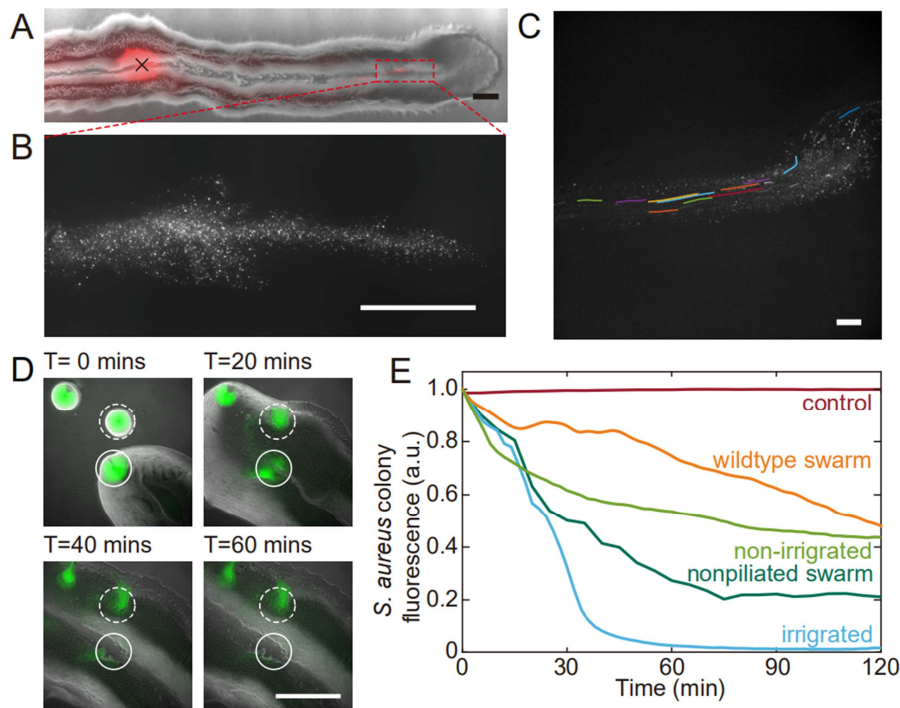
1205 **Fig. 4. Modeling fluid transport and spatial-temporal dynamics of surface tension**
1206 **gradient in canals.** (A) Hydrodynamic simulation of fluid transport in a simplified canal
1207 geometry. The cross-sectional profile of the canal was modeled as a half ellipse with the
1208 major and minor axis being 150 μm and 10 μm , respectively. Note that the vertical and
1209 horizontal length scales are different. Red arrows indicate the direction of surface
1210 tension gradient $\nabla\gamma$. Black arrows and colormap show the surface and the bulk flow
1211 speed profiles, respectively, generated by a surface tension gradient of $1000 \text{ mN} \cdot \text{m}^{-2}$
1212 imposed at the canal's upper surface (liquid-air boundary). (B) Schematic showing the
1213 key processes involved in the establishment of surface tension gradient in canals. Major
1214 constituents of the colony are represented by symbols of different colors: surfactant

1215 molecules, orange dots; QS molecule, blue dots; cells, green rods. The key processes
1216 are labeled by numbers: “1”, transport of bacteria and biosurfactant at the liquid-air
1217 interface driven by surface tension gradient $\nabla\gamma$; “2”, biosurfactant exchange between the
1218 liquid-air interface and the bulk phase; “3”, growth of bacteria and the production of
1219 biosurfactant under QS regulation; “4”, diffusion of biosurfactant, QS molecules, and
1220 nutrient. Arrows indicate the direction of material transport. (C) Schematic showing the
1221 coupling of the key processes described in panel A and in main text. See SI Text for
1222 details. (D,E) Spatiotemporal dynamics of surface-associated surfactant concentration Γ
1223 and surface tension gradient $\nabla\gamma$ obtained by numerical simulations of the mathematical
1224 model, as shown in panels D and E, respectively. Also see Fig. S4 for the numerical
1225 result of the spatial-temporal evolution of other quantities in the model.

1226

1227

1228 Figure 5



1229

1230

1231 **Fig. 5. Fluid flows in *P. aeruginosa* canals transport OMVs and help to eradicate *S.***
1232 ***aureus* colonies.** (A) Phase contrast image of a canal overlaid with the fluorescence
1233 image of OMVs (in red). The cross sign marks the location of microinjecting OMV
1234 dispersion. The loaded OMVs were transported downstream along the canal and
1235 accumulated near the tip. Scale bar, 1 mm. (B) Enlarged view of the OMV fluorescence
1236 image at the red dashed box in panel A. Scale bar, 500 μ m. (C) Colored traces show
1237 the trajectories of fluorescently labeled OMVs during 1-s exposure time. Scale bar, 100
1238 μ m. Also see Movie S10. (D) Image sequence showing the eradication of an *S. aureus*
1239 colony (GFP-labelled, enclosed by the solid line) that was irrigated by *P. aeruginosa*
1240 canal flows. A nearby *S. aureus* colony (enclosed by the dashed line) came into contact
1241 with the *P. aeruginosa* colony but did not encounter canal flows. In each panel the
1242 fluorescence image of *S. aureus* colonies is superimposed onto the phase contrast
1243 image. Also see Movie S11. (E) Temporal dynamics of *S. aureus* colony biomass after
1244 encountering *P. aeruginosa* PA14 colonies under different conditions. To compare with
1245 the effect of potential material transport by flagellar motility (Y. Wu et al., 2011; Xu et al.,
1246 2019), curves labeled as “wildtype swarm” and “nonpiliated swarm” were shown for *S.*
1247 *aureus* colonies encountering wildtype *P. aeruginosa* (with both flagellar and type-IV

1248 pilus motilities) and nonpiliated *P. aeruginosa* (PA14 $\Delta pilB$; with flagellar motility alone),
1249 respectively (see Fig. S6 for details; Methods). At least three replicates were performed
1250 for each condition.

1251

1252

Supplementary Information for

1253

1254 **Self-organized canals enable long range directed material transport in bacterial**
1255 **communities**

1256

1257 Ye Li, Shiqi Liu, Yingdan Zhang, Zi Jing Seng, Haoran Xu, Liang Yang*, Yilin Wu*

1258

1259 *Corresponding authors. Email: ylwu@cuhk.edu.hk or yangl@sustech.edu.cn

1260

1261

1262

1263

1264

1265

1266

This file includes:

1266

1267 Supplementary Text

1268 Figs. S1 to S19

1269 Tables S1 to S2

1270 Legends for Movies S1 to S11

1271

1272 Other Supplementary Information for this manuscript include the following:

1273

1274

1275 **Supplementary Text (SI Text)**

1276

1277 **Mathematical model for the dynamics of surfactant distribution**

1278

1279 A key component of our model for the spatial-temporal dynamics of surfactant
1280 distribution is biosurfactant exchange between the liquid-air interface and the bulk
1281 phase. The kinetics of biosurfactant exchange between the two phases could be
1282 learned from a relation between the bulk concentration and the surface concentration of
1283 biosurfactant at steady state.

1284

1285 Based on our measurement of surface tension at different rhamnolipid concentrations
1286 (Fig. S3), the relation between the steady-state surface tension γ_{ss} and bulk
1287 concentration of biosurfactant c can be well described by an exponential decay:

1288
$$\gamma_{ss}(c) = \Pi_{\max} \exp(-c/c_s) + \gamma_\infty \quad [S1]$$

1289 In Eq. [S1] $\Pi_{\max} = 41.6 \text{ mN} \cdot \text{m}^{-1}$ is the maximal decrease of surface tension; $c_s =$
1290 $12.9 \text{ mg} \cdot \text{L}^{-1}$ is the characteristic concentration of rhamnolipids; $\gamma_\infty = 30.6 \text{ mN} \cdot \text{m}^{-1}$ is
1291 the saturated surface tension of rhamnolipid solutions.

1292

1293 On the other hand, the surface tension directly depends on the surface concentration of
1294 surfactants (Γ). Such a relation is well fitted by a quadratic exponential decay (Hanyak
1295 et al., 2012):

1296
$$\gamma(\Gamma) = \Pi_{\max} \exp(-A\Gamma^2/\Gamma_c^2) + \gamma_\infty \quad [S2]$$

1297 In Eq. [S2], Γ_c is the characteristic surface concentration of surfactant, A is a parameter
1298 relating bulk surfactant concentration to the steady-state surface density of the
1299 surfactant.

1300

1301 Comparing Eq. [S2] to Eq. [S1], we find that $c \sim A\Gamma^2$ at equilibrium. This means that the
1302 surface concentration of rhamnolipids does not saturate but varies with the bulk
1303 concentration. To account for this behavior of rhamnolipids, we model the rate of
1304 biosurfactant transfer (r_{net}) from the bulk phase to the interface as follows:

1305
$$r_{net} \propto \frac{c}{c_s} - A \frac{\Gamma^2}{\Gamma_c^2} = k \left(\frac{c}{c_s} - A \frac{\Gamma^2}{\Gamma_c^2} \right) \quad [S3]$$

1306 In Eq. [S3], k is a reaction rate constant. To simplify the analysis, we introduced the
1307 dimensionless bulk concentration $c_n = c/c_s$ and the dimensionless surface concentration

1308 $\Gamma_n = \Gamma/\Gamma_c$ of rhamnolipids, respectively, and rewrite Eq. [S3]:

1309
$$r_{net} = k(c_n - A\Gamma_n^2) \quad [S4]$$

1310

1311 The spatial-temporal dynamics of the bulk and the interface biosurfactant concentration
1312 c_n and Γ_n are described by the following coupled differential equations:

1313

1314
$$\frac{\partial c_n}{\partial t} = \nabla \cdot (D_c \nabla c_n) - k(c_n - A\Gamma_n^2) + \alpha_R \rho \frac{N}{K_N + N} \frac{B^m}{K_B^m + B^m} \quad [S5]$$

1315
$$\frac{\partial \Gamma_n}{\partial t} = \nabla \cdot (D_\Gamma \nabla \Gamma_n) - \nabla \cdot [\eta_\Gamma \Gamma_n \nabla \gamma(\Gamma_n)] + k(c_n - A\Gamma_n^2) \quad [S6]$$

1316

1317 Here D_Γ , D_c , η_Γ , k , A , K_N , α_R , K_B , K_N , and m are constant parameters whose definitions
1318 and values are described in SI Table S2. Eq. [S5] describes the variation of c_n due to
1319 three processes, namely biosurfactant diffusion in the bulk phase, biosurfactant
1320 exchange between the liquid-air interface and the bulk phase (see Eq. [S4]), and
1321 biosurfactant production. The biosurfactant production term is proportional to bacterial
1322 density (ρ) and bacterial metabolic activity [which is limited by nutrient concentration N
1323 and modeled as a Hill function (Cao et al., 2016), $N/(K_N + N)$], and regulated by the QS
1324 activity (modeled as a Hill function of auto-inducer concentration B with Hill coefficient m
1325 (Cao et al., 2016)); ρ , N and B follow another set of differential equations to be described
1326 below. Eq. [S6] describes the variation of Γ_n due to biosurfactant diffusion at the
1327 interface, advective biosurfactant transport by Marangoni flows, as well as biosurfactant
1328 exchange between the liquid-air interface and the bulk phase. Biosurfactants adsorbed
1329 to the liquid-air interface will be carried by liquid flows in canals, hence giving rise to the
1330 advective transport term in Eq. [S6]. The speed of Marangoni flows in the advective
1331 transport term is proportional to surface tension gradient $\nabla \gamma(\Gamma_n)$ (de Gennes et al.,
1332 2003). Biosurfactant concentration in the bulk phase is assumed to be unaffected by
1333 Marangoni flows because the volume of the bulk phase is much greater than that of the
1334 canals in our experiments.

1335

1336 The spatial-temporal dynamics of N , ρ and B are described by the following coupled
1337 differential equations:

1338

1339
$$\frac{\partial N}{\partial t} = \nabla \cdot (D_N \nabla N) - \beta \frac{N}{K_N + N} \rho \quad [S7]$$

1340
$$\frac{\partial \rho}{\partial t} = \nabla \cdot (D_\rho \nabla \rho) - \nabla \cdot [\eta_\rho \rho \nabla \gamma(\Gamma_n)] + \beta \frac{N}{K_N + N} \rho \frac{1}{1 + \lambda \frac{B^m}{K_B^m + B^m}} \quad [S8]$$

1341
$$\frac{\partial B}{\partial t} = \nabla \cdot (D_B \nabla B) + \alpha_B \rho \frac{B^m}{K_B^m + B^m} + \chi \rho - d_B B \quad [S9]$$

1342

1343 Here D_N , D_ρ , D_B , β , η_ρ , λ , α_B , χ , and d_B are constant parameters whose definitions and
1344 values are described in SI Table S2. The variation of the nutrient concentration field N
1345 (Eq. [S7]) is due to diffusion and consumption, with the nutrient consumption term being
1346 proportional to bacterial density ρ and bacterial metabolic activity $N/(K_N + N)$ as
1347 described above for Eq. [S5]. The variation of the bacterial density field ρ (Eq. [S8]) is
1348 due to three processes, namely diffusion, advective transport by Marangoni flows, and
1349 bacterial growth; the bacterial growth term is proportional to bacterial density ρ and
1350 bacterial metabolic activity, and is repressed by the QS-regulated biosurfactant
1351 production due to the associated metabolic cost. The variation of the QS auto-inducer
1352 concentration field B is described in Eq. [S9]. It includes 4 components, a diffusion term,
1353 a production term proportional to bacterial density ρ and regulated by QS activity via a
1354 Hill function with Hill coefficient m , a basal production term proportional to ρ (to ensure
1355 that autoinduction can be activated), and a degradation term.

1356

1357 Equations [S2, S5-S9] constitute the entire model for the spatial-temporal dynamics of
1358 biosurfactant distribution. All variables in the model are dimensionless. To simplify the
1359 computation we numerically solved Eqs. [S5-S9] in polar coordinate system with
1360 rotational symmetry. The computation was programmed in Fortran and complied by
1361 gFortran 9 on Linux platform. With appropriately chosen model parameters (SI Table
1362 S2), the magnitude of surface tension gradient was tuned to $\sim 1000\text{-}3000 \text{ mN} \cdot \text{m}^{-2}$, so
1363 as to match the estimated magnitude of surface tension gradient (Fig. 4A) required to
1364 generate the observed flow speed in canals (Fig. 3E).

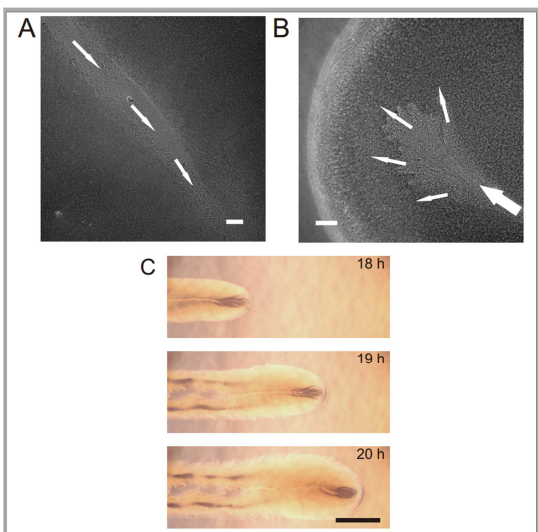
1365

1366

1367 **SI Figures**

1368

1369 **Figure S1**



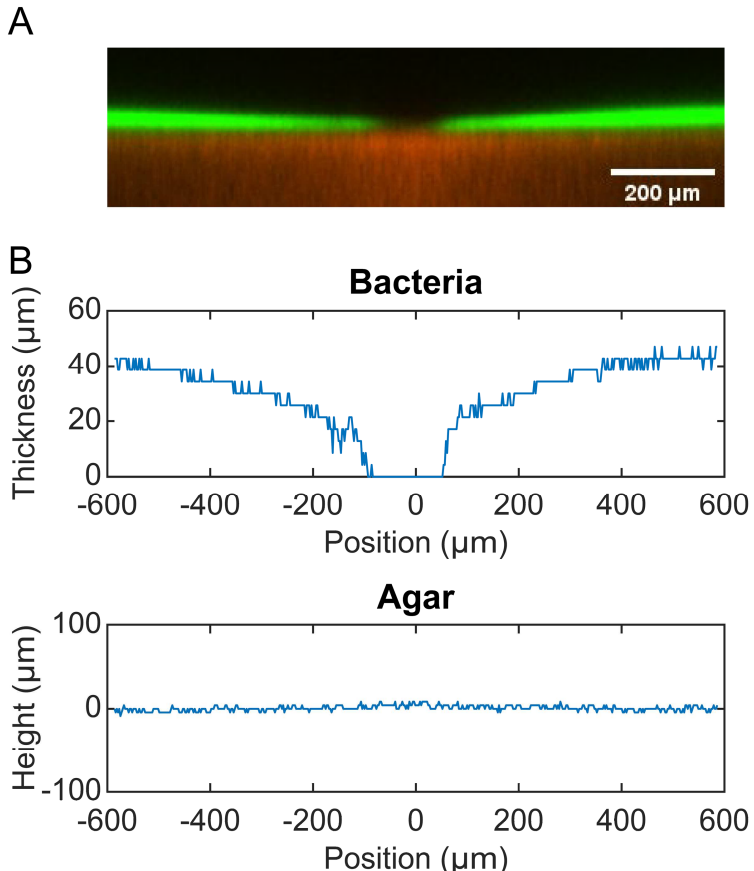
1370

1371 **Fig. S1. Open channels supporting long-range directed material transport in *P.***
1372 ***aeruginosa* colonies.** (A) Phase-contrast microscopy image of an open channel in a *P.*
1373 *aeruginosa* (PA14 *flgK*::Tn5) colony. Arrows indicate the flow direction. Scale bar, 100
1374 μm. Also see Movie S3. (B) Phase-contrast microscopy image taken near the tip of an
1375 open channel in a *P. aeruginosa* (PA14 *flgK*::Tn5) colony. Arrows indicate the flow
1376 direction. Scale bar, 100 μm. Also see Movie S4. (C) Image sequence taken by a
1377 DSLR camera via a 4X phase contrast objective lens showing the development of an
1378 open channel (or canal) in a branching colony of *P. aeruginosa* (PA14 *flgK*::Tn5). Scale
1379 bar, 1 mm. Also see Movie S6. The fluid flow in bacterial canals was sensitive to water
1380 content in the air environment and it was easily disrupted by decrease of humidity. Cells
1381 translocating along the open channels eventually settled in near the colony edge and
1382 they may contribute to colony expansion. Fluid flow in open channels on average went
1383 towards the colony edge and stopped abruptly at the very end (i.e. the tip) of an open
1384 channel, disappearing into the dense layer of cells near the edge (panel B; Movie S4).

1385

1386 Figure S2

1387



1388

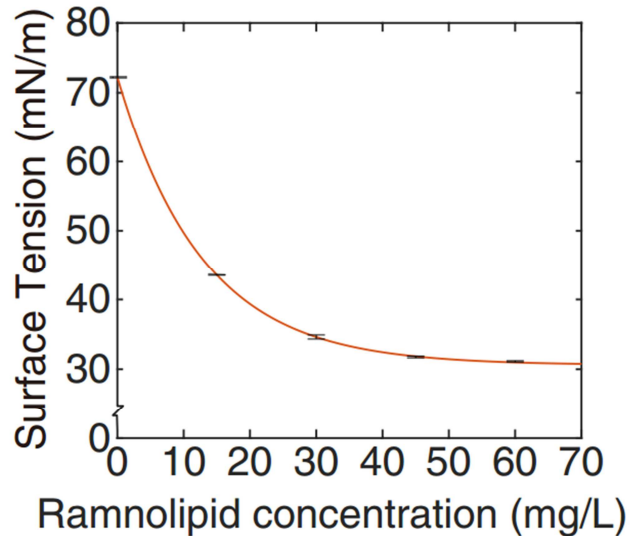
1389

1390 **Fig. S2. Height profiles of colony and agar.** (A) Cross-sectional view of the colony
1391 (green fluorescence) and the agar underneath the colony (red fluorescence) measured
1392 by laser scanning confocal microscopy (see Methods in main text). A canal is located at
1393 the center of the image. (B) Thickness profile of the colony (upper panel) and height
1394 profile the agar underneath the colony (lower panel) associated with panel A. The height
1395 of agar at position 600 μm was chosen as the reference level (i.e., height = 0 μm). The
1396 thickness of the colony is low inside the canal region due to flushing of fluid flows. The
1397 height of agar is uniform, showing that canal formation is not associated with agar
1398 degradation.

1399

1400 Figure S3

1401



1402

1403

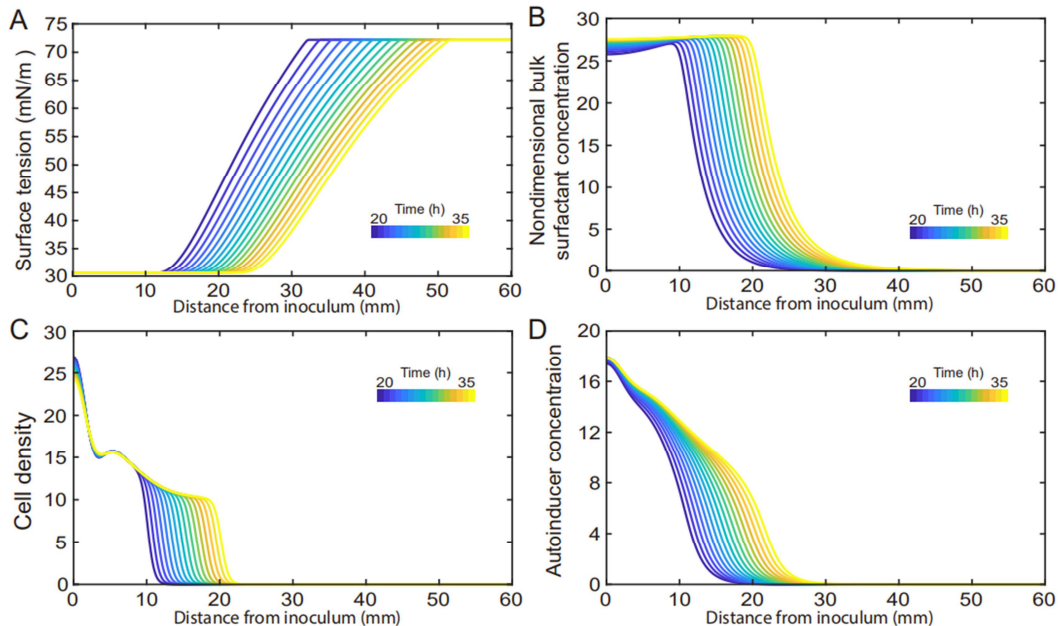
1404 **Fig. S3. Surface tension of rhamnolipid solutions as a function of rhamnolipid**
1405 **concentration.** The relation between bulk rhamnolipid concentration and the steady-
1406 state surface tension. Steady-state surface tension was measured by pendant drop
1407 assay with a commercial contact-angle meter (OCA25, DataPhysics, Germany). The
1408 rhamnolipid solutions were prepared by dissolving rhamnolipids (in solid form) in
1409 M9DCAA medium. Error bars indicate the standard deviation. The line is a fit of data
1410 points to an exponential decay function (Eq. 1 of SI Text).

1411

1412

1413

1414 Figure S4



1415

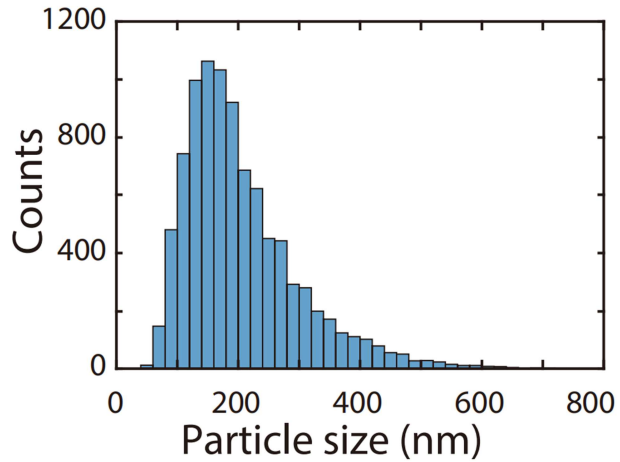
1416 **Fig. S4. Spatial-temporal dynamics of key model variables related to the**
1417 **development of surface tension gradient in canals.** This figure is associated with
1418 main text Fig. 4. The spatial-temporal dynamics of the following variables used in the
1419 model presented in main text and SI were plotted: surface tension, panel (A); bulk
1420 biosurfactant concentration, panel (B); bacterial density, panel (C); autoinducer
1421 concentration, panel (D).

1422

1423

1424 Figure S5

1425

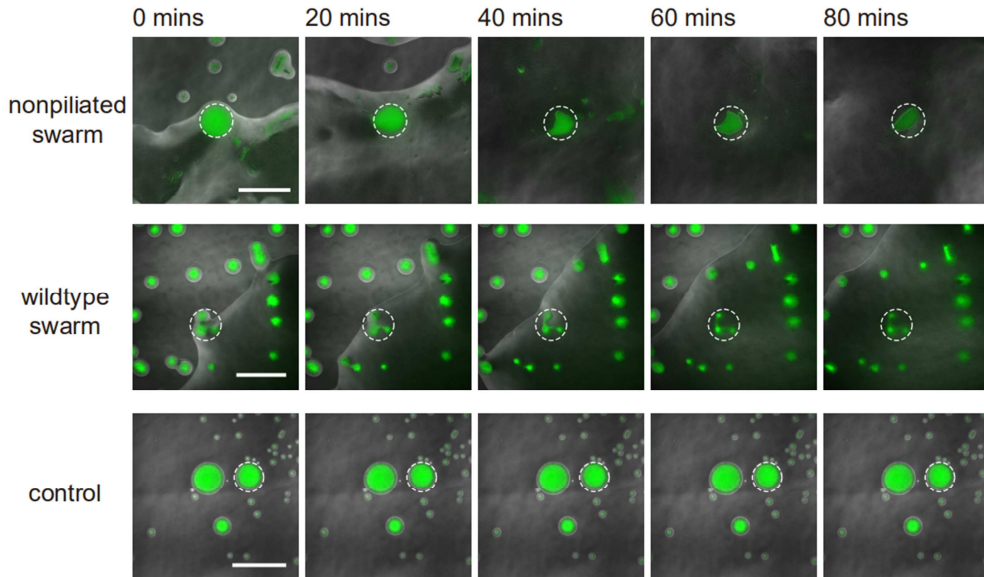


1426

1427 **Fig. S5. Size distribution of outer membrane vesicles (OMVs).** The OMVs were
1428 derived from canal-forming *P. aeruginosa* (PA14 *flgK*::Tn5) and the size distribution was
1429 measured by a particle sizer (NanoSight LM10, Malvern Instruments). See Methods.

1430 Figure S6

1431



1432

1433

1434 **Fig. S6. Interaction between *S. aureus* and *P. aeruginosa* PA14 colonies.** This
1435 figure is associated with Fig. 5, panels D,E. To compare with the effect of potential OMV
1436 transport due to flagellar motility, we co-cultured swarms of flagellated *P. aeruginosa*
1437 PA14 with *S. aureus* colonies under the same conditions as used in Fig. 5D. The image
1438 sequences show the temporal variation of *S. aureus* colony biomass (green
1439 fluorescence) under the following conditions: top, in contact with the swarming colony of
1440 PA14 $\Delta pilB$ mutant; middle, in contact with the swarming colony of wildtype PA14;
1441 bottom, control experiment in the absence of *P. aeruginosa*. Both PA14 $\Delta pilB$ mutant
1442 and wildtype PA14 have flagellar motility, but neither of them can form canals. In each
1443 panel the fluorescence image of *S. aureus* colonies (green) is superimposed onto the
1444 phase contrast image. The dashed circles mark the region with *S. aureus* colonies for
1445 fluorescence analysis in Fig. 5E. As shown in main text Fig. 5E, the *S. aureus* colonies
1446 encountering expanding *P. aeruginosa* swarms were destructed to a lesser extent
1447 compared to the case that were irrigated by canal flows, retaining ~20% and ~50% of
1448 cell mass after 60 min of contact with swarming colonies of *P. aeruginosa* PA14 $\Delta pilB$
1449 mutant and wildtype PA14, respectively.

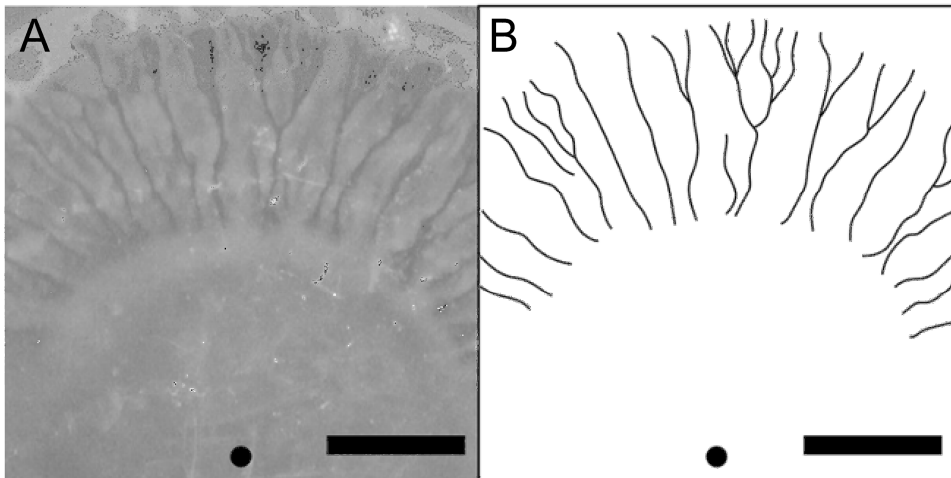
1450

1451

1452

1453 Figure S7

1454



1455

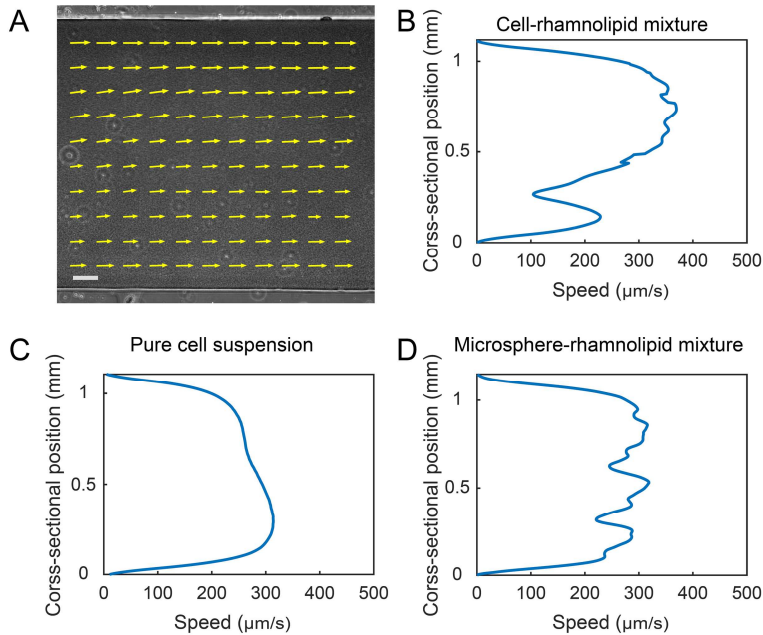
1456

1457 **Fig. S7. Canal formation in *Serratia marcescens* colonies.** Overnight culture of *S.*
1458 *marcescens* grown in LB medium was inoculated on 0.6% Eiken agar plates and
1459 photographed in a custom-built imaging incubator made of PMMA. The temperature of
1460 the incubator was maintained at 30 °C and the images of canals were photographed by
1461 a digital single-lens reflex camera. (A) Canal appeared ~4 h after colony inoculation.
1462 (B) Sketch of the canals in panel A for better visualization. The black dot represents the
1463 inoculum. Scale bars, 500 μm .

1464

1465 Figure S8

1466



1467

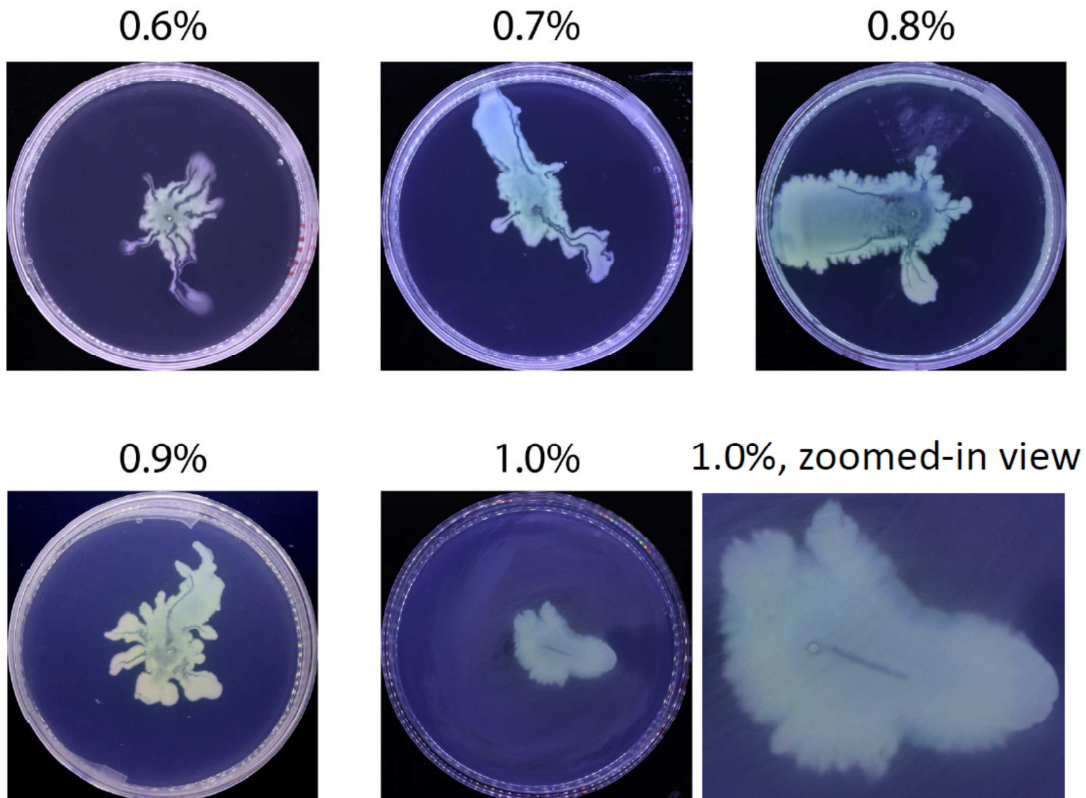
1468 **Fig. S8. Shear banding of cell-rhamnolipid mixture in PDMS microfluidic**
1469 **channels.** (A) Flow velocity field of cell-rhamnolipid mixture in a microfluidic channel.
1470 The microfluidic channel had a rectangular cross-section (200 μm of height, 1.1 mm of
1471 width). Cells (PA14 *flgK*::Tn5; ZK3367) and rhamnolipids were mixed at a final density
1472 (concentration) of 1.9×10^{10} cells/mL and 10 mg/mL, respectively, and driven by a syringe
1473 pump at a flow rate of 5 mL/min. The velocity field was measured by PIV analysis on
1474 phase-contrast image sequence and averaged over a time window of 5 s. The velocity
1475 field is superimposed onto one of the analyzed phase-contrast images. Arrows indicate
1476 velocity vectors. Scale bar, 100 μm. (B) Cross-sectional flow speed profile computed
1477 based on velocity field data shown in panel A. Each data point represents local velocity
1478 averaged in a domain of 41.6 μm x 41.6 μm centered around the cross-sectional position.
1479 (C,D) Cross-sectional flow speed profile in microfluidic channels filled with other fluids.
1480 Data in panel C was obtained with pure cell suspension (1.9×10^{10} cells/mL), and data in
1481 panel D with a mixture of rhamnolipids (10 mg/mL) and 1.1-μm microsphere suspension
1482 ($\sim 1.9 \times 10^{10}$ particles/mL). These fluids were driven through microfluidic channels by a
1483 syringe pump at a flow rate of 3 mL/min. The flow speed profiles were computed based
1484 on the respective time-averaged velocity field, which was obtained by PIV analysis on
1485 phase-contrast image sequence and averaged over a time window of 5 s. Each data

1486 point in C,D represents local velocity averaged in a domain of 41.6um x 41.6um
1487 centered around the cross-sectional position. See Methods for details of experiments
1488 and image analysis associated with all panels.

1489

1490 Figure S9

1491



1492

1493 **Fig. S9. Representative images of canal development at different agar**
1494 **concentrations.** The colonies were from the same batch and incubated under the
1495 same condition (30 °C) for the following durations: 0.6%-0.8%, 19 hr; 0.9%, 24 hr; 1.0%,
1496 36 hr. Canals can be found in different agar (infused with M9DCAA medium)
1497 concentrations from 0.6% to 1.0%, in addition to the 0.5% agar used in the main text.
1498 Note that a canal in the colony on the 1.0% plate is located at the center (see the
1499 zoomed-in view).

1500

1501 **SI Tables**

1502

1503 Table S1. Primers

1504

No.	Oligo Name	Sequence 5' to 3'
1	1-rhlA_UpF	agctcggtaccgggGGGTGATTCTACGGGGTG
2	2-rhlA_UpR	CTTCGCAGGTCAAGGGTTACCGCATTACACCTCCAA
3	3-rhlA_DownF	TTGGGAGGTGTGAAATGCGGTGAACCCTGACCTGCGAAG
4	4-rhlA_DownR	cgacggccagtgcacCCGTACTTCTCGTGAGCGAT
5	rhlA_F	GACAAGTGGATTGCCGCA
6	rhlA_R	TTGAACTTGGGTGTACCGG
7	rhlAGENE_F	GGTCAATCACCTGGTCTCCG
8	rhlAGENE_R	GCTGATGGTTGCTGGCTTTC
9	Pk18-F	TGCTTCCGGCTCGTATGTTG
10	Pk18-R	GCGAAAGGGGGATGTGCTG

1505

1506

1507 Table S2. Simulation parameters

1508

Parameter	Description	Value	Unit	Robust range [#]
α_R	Biosurfactant synthesis rate	2×10^{-3}	s ⁻¹	$5 \times 10^{-4} - 1 \times 10^{-2}$
β	Bacterial growth rate	6×10^{-4}	s ⁻¹	$3 \times 10^{-4} - 1 \times 10^{-3}$
K_N	Nutrient concentration for half maximal metabolic activity	1	Nondimensional	N/A
K_B	Half-activation threshold of QS auto-inducer	1	Nondimensional	N/A
α_B	Auto-inducer	2×10^{-4}	s ⁻¹	$1 \times 10^{-4} - 1 \times 10^{-3}$

	synthesis rate			
d_B	Auto-inducer degradation rate	2×10^{-4}	s^{-1}	$0 - 2 \times 10^{-4}$
χ	Auto-inducer basal production rate	2×10^{-6}	s^{-1}	$1 \times 10^{-6} - 2 \times 10^{-5}$
m^*	Hill coefficient of QS regulation	2		N/A
λ	Parameter of growth-repression due to QS-regulated biosurfactant production	0.3	Nondimensional	0-0.5
k^{**}	Reaction rate constant for biosurfactant transfer between the bulk phase and the interface	2×10^{-5}	s^{-1}	N/A
A^{***}	Ratio between bulk surfactant concentration and square of the steady-state surface density	6.125	Nondimensional	2-10
η_ρ^{**}	Parameter of advective bacterial transport	5×10^{-11}	$(mN \cdot m^{-2})^{-1}s^{-1}$	N/A
η_Γ^{**}	Parameter of advective biosurfactant transport	2.5×10^{-10}	$(mN \cdot m^{-2})^{-1}s^{-1}$	N/A
D_c	Diffusion coefficient of biosurfactant in	1×10^{-9}	$m^2 s^{-1}$	$0 - 1 \times 10^{-9}$

	bulk phase			
D_Γ	Diffusion coefficient of biosurfactant at liquid-air interface	5×10^{-11}	m^2s^{-1}	$0 - 1 \times 10^{-10}$
D_ρ	Diffusion coefficient of bacteria	5×10^{-11}	m^2s^{-1}	$0 - 5 \times 10^{-11}$
D_B	Diffusion coefficient of auto-inducers	1×10^{-9}	m^2s^{-1}	$5 \times 10^{-10} - 1 \times 10^{-9}$
D_N	Diffusion coefficient of nutrient	1×10^{-9}	m^2s^{-1}	$0 - 2 \times 10^{-9}$

1509

1510 # The results shown in main text Fig. 4D,E are robust to variation of parameters within
1511 the indicated range.

1512 * The value of this parameter is taken from reference (Payne et al., 2013).

1513 ** These parameters are chosen to yield the width of the plateau of surface tension
1514 gradient distribution (Fig. 4D) being ~25 mm (matching the experimental results).

1515 *** The value of this parameter is taken from reference (Hanyak et al., 2012).

1516 **Legends of SI Movies**

1517

1518

1519 Movie S1. Rapid cellular flow streaming through a nonpiliated *P. aeruginosa* (PA14
1520 $\Delta pilB$) colony. Cells are motile outside the stream.

1521

1522

1523

1524 Movie S2. Cellular flow in an open channel of non-motile *P. aeruginosa* (PA14 $flgK::Tn5$
1525 $\Delta pilA$) colony. This real-time video is associated with Fig. 1E in main text.

1526

1527

1528

1529 Movie S3. Cellular flow in an open channel of a pilated *P. aeruginosa* (PA14 $flgK::Tn5$)
1530 colony. This real-time video is associated with Fig. S1, panel A.

1531

1532

1533

1534 Movie S4. Cellular flow near the tip of an open channel in a pilated *P. aeruginosa* (PA14
1535 $flgK::Tn5$) colony. The flow slowed down and stopped abruptly at the tip, disappearing
1536 into the dense layer of cells near the edge of the colony. Note that the colony edge had
1537 ceased expansion and in general, canal formation does not necessarily coincide with
1538 colony expansion. This real-time video is associated with Fig. S1, panel B.

1539

1540

1541

1542 Movie S5. Development of open channels in branching colonies of pilated *P.*
1543 *aeruginosa* (PA14 $flgK::Tn5$). The colony was grown on M9DCAA agar plates at 30 °C.
1544 Time label shows the elapsed time from inoculation (hh:mm). The video is associated
1545 with Fig. 1F in main text.

1546

1547

1548

1549 Movie S6. Zoomed-in view of a developing bacterial canal in a branching colony of

1550 piliated *P. aeruginosa* (PA14 *flgK*::Tn5). Time label shows the elapsed time from
1551 inoculation (hh:mm). The video is associated with Fig. S1, panel C.

1552

1553

1554

1555 Movie S7. Effect of externally applied counteracting surface tension gradient on fluid
1556 transport in canals. An agar patch infused with surfactant TWEEN 20 (50 mg/mL) was
1557 placed at ~1 cm in front of a colony branch of piliated *P. aeruginosa* (PA14 *flgK*::Tn5);
1558 see Methods. As shown in the video, immediately following this operation, fluid flows in
1559 the canal gradually ceased and the canal slowly retracted. Time label shows the
1560 elapsed time from placing the agar patch (mm:ss).

1561

1562

1563

1564 Movie S8. Distinct flow regimes occurring in a homogeneous region of a piliated *P.*
1565 *aeruginosa* (PA14 *flgK*::Tn5) colony. The video is associated with Fig. 3A,B in main text.

1566

1567

1568

1569

1570 Movie S9. The course of a developing canal in a colony. Cells in the colony hosted a
1571 plasmid expressing the rhamnolipid synthesis reporter P_{rhlA} -*gfp*(ASV) and the colony was
1572 imaged by fluorescence microscopy. Scale bar, 125 μ m. Time label is in the format of
1573 hh:mm:ss. The video is associated with Fig. 3C in main text.

1574

1575

1576

1577 Movie S10. Transport of outer membrane vesicles (OMVs) along a canal. This real time
1578 video records at 10 frames per second the fluorescence of FM1-43 FX labeled OMVs
1579 that were being transported along a canal in a *P. aeruginosa* (PA14 *flgK*::Tn5) colony.
1580 Purified OMVs was injected into the canal at ~15 mm upstream from the tip of the canal,
1581 and the video was acquired after ~2 min at ~5 mm upstream from the tip of the canal.
1582 The video is associated with Fig. 5C in main text.

1583

1584

1585

1586 Movie S11. Eradication of an *S. aureus* colony irrigated by *P. aeruginosa* canal flows. *S.*
1587 *aureus* (with constitutive GFP expression) colonies were co-cultured with *P. aeruginosa*
1588 (PA14 *flgK*::Tn5); see Methods. Time label (in hh:mm format) shows the elapsed time
1589 from full contact between the *P. aeruginosa* colony and the *S. aureus* colony near the
1590 center. The fluorescence image of *S. aureus* colonies is displayed in logarithmically
1591 transformed pixel values, in order to accommodate the broad dynamic range. In each
1592 video frame the fluorescence image is superimposed onto the corresponding phase
1593 contrast image acquired simultaneously. As shown in the video, the *S. aureus* colony
1594 irrigated by *P. aeruginosa* canal flows was quickly eradicated, while a nearby *S. aureus*
1595 colony that came into full contact with the *P. aeruginosa* colony but did not encounter
1596 canal flows retained ~40% colony biomass after ~60 min. The video is associated with
1597 Fig. 5D in main text.